Revision 1

Multi-stage barite crystallization in partially melted UHP eclogite from the Sulu belt, China

SONGJIE WANG[1, 2], LU WANG[1, 2*], MICHAEL BROWN[2, 3] AND PENG FENG[1]

[1]State Key Laboratory of Geological Processes and Mineral Resources, School of Earth Sciences, China University of Geosciences, Wuhan, 430074, China

[2]Center for Global Tectonics, School of Earth Sciences, China University of Geosciences, Wuhan, 430074, China

[3]Laboratory for Crustal Petrology, Department of Geology, University of Maryland, College Park, MD 20742, USA

ABSTRACT

Barite inclusions in rock-forming and accessory minerals and in multiphase solid inclusions (MSI) in ultrahigh pressure (UHP) eclogites have been controversially interpreted to record the presence of high-salinity oxidizing fluids[1] close to the peak of metamorphism. A detailed petrographic and microstructural study of barite in partially melted UHP eclogite from Yangkou, in the central Sulu belt of China demonstrates that barite precipitation is a multi-stage process and provides insight into the evolution of fluid systems as *P–T* conditions evolved through the

[1]In this article we use fluid as a general term for an aqueous fluid phase, a supercritical fluid phase and a melt phase. Where these phases are distinguished, we use the specific term as appropriate.

late prograde stage of subduction to the peak of UHP metamorphism and subsequently during exhumation. Five microstructural types of barite are recognized in this study. Type I barite (variable high to low Sr/Ba) occurs as equant primary inclusions with rutile in garnet and omphacite within coesite-bearing eclogite. Zr-in-rutile thermometry on the primary inclusions of rutile yields T = 658–699 ^{o}C at P = 2.5–4.5 GPa. Thus, barite inclusions were likely precipitated from an internally buffered fluid during the late prograde evolution. Type II barite (low Sr/Ba) occurs in MSI located towards the rims of garnet and omphacite. Since peak pressure was above the second critical endpoint for basaltic compositions, the MSI are inferred to represent aliquots of silica-rich supercritical fluid trapped during the late prograde evolution close to the metamorphic peak. Type III barite (low Sr/Ba) occurs in pseudomorphs after phengite inclusions in garnet. The replacement phase assemblage formed during exhumation, by *in situ* melting of phengite. Type IV barite (low Sr/Ba) forms coarse-grained patches associated with sub-solidus replacement of omphacite by hornblende and albite symplectites along grain boundaries. Type V barite (low Sr/Ba) occurs as grain-boundary veinlets, intergranular grains and closed rings around pyrite that is partly replaced by hematite and goethite. We interpret the types IV and V barite to have precipitated from an internally generated grain-boundary aqueous fluid, which is expected to be a response to H_2O exsolving from garnet and omphacite during low-pressure amphibolite facies conditions. Therefore, barite precipitated during the late prograde subduction and the retrograde exhumation of UHP eclogite yields information about the mobility of Ba, Sr and S during the metamorphic evolution.

Keywords: barite, multiphase solid inclusions, supercritical fluid, partial melting, melt/fluid immiscibility, UHP eclogite, Sulu belt

INTRODUCTION

Ultrahigh pressure (UHP) metamorphic rocks record evidence of processes related to deep subduction and exhumation of continental crust. During UHP metamorphism, fluid plays an important role in facilitating mineral reactions, element mobility, crust–mantle interactions and exhumation (e.g., Zhang et al. 2011; Zheng et al. 2011b; Sizova et al. 2012; Hermann et al. 2013; Zheng and Hermann 2014; Frezzotti and Ferrando 2015). Various studies have investigated: (1) HP–UHP metamorphic veins (e.g., Franz et al. 2001; Zheng et al. 2007; John et al. 2008; Zhang et al. 2008); (2) hydrous minerals, such as epidote, lawsonite, amphibole and phengite (e.g., Guo et al. 2012, 2014; Sheng et al. 2013; Brovarone et al. 2014a, b; Martin et al. 2014); (3) fluid inclusions (e.g., Philippot and Selverstone 1991; Philippot et al. 1995; Scambelluri and Philippot 2001); (4) multiphase solid inclusions (e.g., Ferrando et al. 2005; Zheng et al. 2011b; Ferrero et al. 2015); and, (5) the exsolution of hydroxyl and molecular water from nominally anhydrous minerals (e.g., Xia et al. 2005; Chen et al. 2007, 2011; Sheng et al. 2007; Sakamaki and Ogasawara 2014).

However, in many circumstances, the source, nature and behavior of the fluid remain controversial due to its multi-generational character (Yardley et al. 2000; Spandler and Hermann 2006; Chen et al. 2007; Zheng 2009; Zong et al. 2010; Spandler et al. 2011; Zheng et al. 2011b; Guo et al. 2014; Frezzotti and Ferrando 2015). This is especially so in circumstances where fluid

generation and evolution are related to decompression from UHP conditions, during which process the *P–T* path may cross into the suprasolidus field. Many previous studies of melting in crustal rocks have focused on melt generation and transfer, and the timing and geological significance of partial melting for tectonics (e.g., Wallis et al. 2005; Brown et al. 2011; Labrousse et al. 2011, 2015; Sizova et al. 2012; Brown 2013; Yakymchuk et al. 2013; Wang et al. 2014; Yakymchuk and Brown 2014). By contrast, experimental studies of melt generation at UHP conditions (Auzanneau et al. 2006; Liu et al. 2009), and consideration of the role of supercritical fluid at pressures above the second critical endpoints (Manning 2004), which are located around 2.5 GPa/700 °C and 3.4 GPa/770 °C for felsic and mafic rocks, respectively (Hack et al. 2007; Mibe et al. 2011), and melt/aqueous fluid separation and evolution during exhumation at lower pressures (Zheng et al. 2011b; Zheng and Hermann 2014; Frezzotti and Ferrando 2015) have lagged behind.

Barite in UHP metamorphism

On contemporary Earth, barite is found principally in deep-sea sedimentary environments, and in biogenic, hydrothermal and evaporite systems (Hanor 2000). By contrast, the principal geological occurrences of barite are in laminated sedimentary rocks and as a gangue mineral in hydrothermal metalliferous veins (Chang et al. 1996). Although barite is known from metamorphic rocks, it has received less attention in this setting, and the principal examples represent metamorphosed equivalents of black shale-hosted submarine exhalative deposits (e.g., Coats et al. 1980; Fortey et al. 1993; Kribek et al. 1996). However, during the past fifteen years

barite has been reported with increasing frequency as an accessory mineral in metamorphic rocks associated with deep subduction, particularly from UHP localities in the Dabie–Sulu belt.

In the Dabie–Sulu belt, barite occurs most commonly as inclusions in garnet, omphacite or zircon or in multiphase solid inclusions (MSI) in these minerals (Liu et al. 2000, 2001; Yang et al. 2006, 2010; Zeng et al. 2007; Gao et al. 2012, 2014a; Chen et al. 2014; Wang et al. 2014). The occurrence of barite as inclusions and in MSI is evidence of a high-salinity oxidizing fluid contemporaneous with UHP metamorphism (Frezzoti and Ferrando 2015). Commonly barite precipitation has been related to a single fluid event during the prograde, peak or retrograde segment of the *P*–*T* evolution.

Liu et al. (2000, 2001), who were the first to recognize barite as inclusions in zircon from gneisses in the eastern Dabieshan, inferred the presence of a SO_4^{2-}-bearing fluid derived by oxidation of sulfide minerals at the peak of UHP metamorphism. Subsequently, Ferrando et al. (2005) identified barite in MSI in quartzite from Donghai in the southern Sulu belt. These authors interpreted the MSI as remnants of a silica-rich supercritical fluid inferred to have been in equilibrium with the peak metamorphic mineral assemblage at UHP conditions.

In the first of several studies of UHP eclogite from the Chinese Continental Scientific Drilling (CCSD) main borehole southwest of Donghai, Yang et al. (2006, 2010) related Sr-rich barite inclusions in garnet, barite with variable Sr in symplectites of clinopyroxene and albite, and barite asociated with the oxidized rims of pyrite to the activity of a variably oxidized fluid. Also in samples from the CCSD main borehole, Zeng et al. (2007) recognized isolated barite grains within K-feldspar or quartz in K-feldspar–quartz intergrowths that pseudomorph

inclusions of a precursor mineral in omphacite in UHP eclogite. The intergrowths were interpreted as the product of a potassium-rich fluid interacting with coesite, but Zeng et al. (2007) argued that barite was present as primary inclusions in the coesite. Thus, they interpret barite to have been precipitated from an oxidizing fluid during prograde metamorphism.

Sun et al. (2007) studied apatite aggregates in quartz veins that cut quartz eclogites retrieved from the CCSD main borehole. The apatite contains exsolved platy monazite, needle-like hematite and strontian barite, and irregular magnetite/hematite intergrowths, implying that the oxygen fugacity was above the sulfide–sulfur oxide buffer. Thus, the veins were deposited from oxidizing SiO_2-rich aqueous fluids. Chemical dating of the monazite yielded an age of 202 ± 28 Ma, providing a minimum age for the vein-forming event, which was most likely post-peak, and demonstrating that exsolution was related to exhumation.

Gao et al. (2012, 2014a), in UHP eclogite from Dabieshan, and Chen et al. (2014), in UHP eclogite from Qinglongshan in the southern Sulu belt, report barite-bearing MSI in garnet and omphacite. Gao et al. (2014a) presented evidence for the co-existence of silicate and carbonate melts, and argued that the MSI with barite were crystallized from composite silicate–carbonate melts. By contrast, Chen et al. (2014) argued that barite-free MSI were generated by paragonite-breakdown melting, whereas they interpreted barite-bearing MSI to have formed by melting of Ba-rich phengite and spatially-related barite-filled cracks to record interaction between a consanguineous aqueous fluid and the host mineral.

These different interpretations of the timing and mechanism of barite precipitation suggest there is still much to be learned about fluid-related processes during UHP metamorphism.

Moreover, multi-stage barite precipitation provides an opportunity to trace the evolution of the fluid accompanying metamorphism during the late prograde and retrograde segments of the *P–T* path. Here we present the results of a detailed petrographic, microstructural and chemical study of barite from eclogite at Yangkou in the central part of the Sulu belt (Fig. 1), supported by Zr-in-rutile thermometry, Ti-in-zircon thermometry and geochemistry. The UHP eclogite at Yangkou is unique as the only example where intergranular coesite, in contrast to coesite as inclusions in zircon and rock-forming minerals, is preserved from the metamorphic peak (Liou and Zhang 1996; Ye et al. 1996). Furthermore, the peak mineral assemblage does not include phengite (Wang et al. 2014). These observations suggest that at least locally the rock was fluid-absent at the metamorphic peak and, further, that any post-peak fluid migration must have been limited and heterogeneously distributed. In addition, the outcrops at Yangkou preserve grain-scale evidence of partial melting, which Wang et al. (2014) argued occurred during exhumation. Accordingly, the Yangkou locality is a suitable target to investigate potentially closed-system fluid evolution related to processes associated with metamorphism during continental subduction and exhumation.

GEOLOGICAL SETTING AND SAMPLES

The Dabie–Sulu orogen in east–central China was formed by northward subduction and collision of the Yangtze block beneath the North China block during the Triassic, after which the NNE-trending Sulu belt was displaced northward by approximately 500 km of sinistral offset along the Tan-Lu fault (Figs. 1a and 1b; Li et al. 1993; Ernst et al. 2007; Hacker et al. 2009; Ni et

al. 2013; Wu and Fu 2014). The Sulu UHP belt consists of mainly orthogneiss and paragneiss, with minor coesite-bearing eclogite, garnet peridotite, quartzite and marble, all of which are intruded by Mesozoic granites (Zhang et al. 1995; Liu et al. 2004; Xu et al. 2006; Li et al. 2014). Coesite occurs widely in eclogite and as inclusions in zircon from associated gneisses, quartzite and marble (Liu and Liou 2011, and references therein). SHRIMP U–Pb dating of coesite-bearing domains in zircon from eclogite and gneiss yielded ages of 234 ± 4 to 225 ± 2 Ma (Liu and Liou 2011), indicating that all units record the Triassic UHP metamorphism.

This study is located in the central Sulu belt at Yangkou (Fig. 1b), where the coastal outcrop is composed of metagabbro, partially retrogressed coesite-bearing eclogite, and serpentinized garnet peridotite. The mafic–ultramafic rocks are surrounded by quartzo-feldspathic gneisses and cut by lamprophyre and quartz porphyry dikes (Fig. 1c). The mafic rocks preserve partially transitional relationships from protolith gabbro to UHP eclogite, as documented by detailed petrological, geochronological and isotope studies (Wallis et al. 1997; Zhang and Liou 1997; Chen et al. 2002; Liu and Liu 2009). Ye et al. (2000) recognized clinopyroxene, rutile and apatite exsolution in garnet from eclogite blocks within surrounding UHP peridotites, implying continental subduction to a depth possibly > 200 km.

The eleven samples chosen for this study are located in Fig. 1c. The samples include four eclogites with intergranular coesite (YK24b, YK5-2a, YK137-8 and YK128-4-1), four quartz eclogites (YK12-3a, YK128-11, YKN149-4 and YKN149-5) and three orthogneisses (YK137-1, YK137-16 and YK137-17). The orthogneisses were included in the study to allow comparison between them and the eclogites, as well as with the protolith metagabbros using data from the

literature to investigate elemental mobility during deep continental subduction and exhumation, particularly in relation to the large ion lithophile elements (LILEs).

ANALYTICAL METHODS

Samples collected for geochemistry weighed 4–5 kg each and comprised sufficient fresh material to be considered representative for all whole-rock analytical methods used in this study. The major element composition of minerals was determined using JEOL JXA-8800R and JEOL JXA-8100 Electron Probe Micro Analyzers (EPMA) at the Institute of Mineral Resources, Chinese Academy of Geological Sciences (IMR-CAGS) in Beijing and the State Key Laboratory of Geological Processes and Mineral Resources (SKLGPMR), China University of Geosciences (CUG), Wuhan, respectively. The analytical conditions in both cases were an acceleration voltage of 15 kV, with a 20 nA beam current, a 1-5 μm beam spot diameter and a count time of 15-20 s; matrix corrections were carried out using the ZAF correction routine supplied by the manufacturer. Mineral standards (from SPI Supplies Inc.) used for calibration of the JEOL JXA-8800R EPMA in IMR-CAGS were jadeite (Na, Si, Al), microcline (K), wollastonite (Ca), hematite (Fe), barite (Ba), and celestine (Sr), whereas those used for the JEOL JXA-8810 EPMA in SKLGPMR at CUG were sanidine (K), pyrope garnet (Al, Fe), diopside (Mg, Ca), jadeite (Na, Si), rhodonite (Mn), barite (Ba, S) and celestine (Sr).

The grain size of the rutile inclusions is too small for analysis of Zr by LA-ICP-MS. Therefore, the EPMA at the IMR-CAGS was also used to determine trace element concentrations of rutile *in-situ* in polished thin sections. According to Gao C.G. et al. (2010), the precision of Zr

187 analysis by EPMA is within 5 % of results determined by LA-ICP-MS. To achieve a lower
188 detection limit for trace element analysis, a strategy combining a higher acceleration voltage of
189 20 kV, a higher beam current of 100 nA, a beam diameter of 1 μm and an extended counting time
190 of 300 s (Zr), 400 s (Nb) and 60 s (Fe), with optimization of the background peak positions was
191 adopted. For analysis of Zr, Nb and Fe, the crystals used were PETH, PETJ and LiFJ,
192 respectively; the detection limits were 20 ppm (Zr), 27 ppm (Nb) and 43 ppm (Fe). Calibration of
193 Zr using a ZrO_2 standard was conducted before, during and after each analysis, and the resulting
194 analytical uncertainty for Zr was determined to be ~15 ppm.
195 All other analytical data were collected at the SKLGPMR, CUG, Wuhan. Back-scattered
196 electron (BSE) imaging, electron back-scattered diffraction (EBSD) for crystal orientation
197 mapping, and energy dispersive spectroscopy for mineral identification were undertaken using a
198 FEI Quanta 450 field emission gun scanning electron microscope (accelerating voltage 20 kV
199 and spot size 6.0 μm with a working distance of ~12 mm).
200 Barite, iron oxide and sulfide were analyzed using a Renishaw RM 1000 Raman
201 spectrometer at room temperature with 3.4 mw of 514.5 nm Ar laser excitation over the spectral
202 range 1000–3800 cm^{-1}. We used a laser beam of ~1.5 μm diameter, a spectrometer grating of
203 1800 gr/mm, an acquisition time of 30 s, and 1–3 cycles. Calibration was performed using
204 monocrystalline silicon. The estimated spectral resolution is 0.5 cm^{-1}.
205 Whole-rock trace element concentrations were acquired using an Agilent 7500a ICP-MS
206 (inductively coupled plasma mass spectrometer). Whole-rock samples were crushed in a
207 corundum jaw crusher to < 60 mesh. About 60 g was powdered in an agate ring mill to < 200

mesh. The powdered sample was digested in HF + HNO_3 using Teflon bombs. The detailed sample-digestion procedure for ICP-MS analysis and a discussion of analytical precision and accuracy for trace element analysis are given by Liu et al. (2008).

Trace element concentrations in zircon were measured by LA-ICP-MS synchronously with analysis for U–Pb geochronology. Operating conditions for the laser ablation system and the ICP-MS instrument, and data reduction protocol are the same as those of Liu et al. (2008). Samples were ablated using a GeoLas 2005 laser, which was connected to an Agilent 7500a ICP-MS instrument to acquire ion-signal intensities using the Agilent Chemstation. Helium was the carrier gas and argon was used as the make-up gas, which was mixed with the carrier gas via a T-connector before entering the ICP. Nitrogen was added into the central gas flow of the Ar plasma to decrease the detection limit and improve precision (cf. Hu et al. 2008). Each analysis incorporated a background acquisition of approximately 20 s (gas blank) followed by 50 s data acquisition from the sample. Off-line selection and integration of background and analyte signals, and time-drift correction and quantitative calibration for trace element concentrations and U–Pb analysis were performed using *ICPMSDataCal* (Liu et al. 2008).

SUMMARY OF THE METAMORPHIC EVOLUTION AT YANGKOU

The mineral assemblages in the eclogites at Yangkou preserve a relatively complete history of late prograde subduction, exhumation and amphibolite facies retrogression (Wang et al. 2014). Mineral names are abbreviated according to the recommendations of Whitney and Evans (2010).

The late prograde to peak mineral assemblage in eclogite comprises Grt + Omp + Coe + Py + Zrn + Ap + Rt, with barite as inclusions in garnet and omphacite but without phengite, similar to the diamond eclogite facies mineral assemblage recognized in the Kokchetav UHP metamorphic terrane (Katayama et al. 2006). Although pressure could have been as high as 7 GPa for the peak mineral assemblage (Ye et al. 2000), Wang et al. (2014) calculated temperatures of > 800 and < 1000 ^{o}C for the more conservative pressure of 3.5–6.0 GPa.

During the early stage of exhumation, phengite appears in the mineral assemblage as fluid is exsolved from nominally anhydrous minerals; concomitantly, the amount of intergranular coesite is reduced. For the mineral association Grt + Omp + Ph, Wang et al. (2014) calculated *P* of 3.7–3.3 GPa and *T* of 753–725 ^{o}C. With continued exhumation across the Coe → Qz phase change, phengite increases in the mode. The eclogite at this stage comprises Grt + Omp + Qz + Ph (~10–15 vol%) + Bt + Rt + Ap + Py/Hem. For a pressure of 2.5 GPa, just in the Qz stability field, Wang et al. (2014) calculated *T* of 700–770 ^{o}C for this assemblage. The retrogressed eclogite is characterized by an amphibolite facies mineral assemblage of Grt (+ relict Omp) + Hb + Qz + Ilm + Ap + Py/Hem + symplectite (Hb + Ab) associated with Brt; phengite is absent and is inferred to have been eliminated during decompression partial melting (Wang et al. 2014).

MICROSTRUCTURAL SETTING AND PETROGRAPHIC CHARACTERISTICS OF BARITE IN UHP ECLOGITE

Barite is present in five distinct microstructural settings, as described below.

Barite inclusions in garnet and omphacite in the coesite and quartz eclogite

Type I barite occurs as equant inclusions within the central domains of garnet and omphacite where it co-exists with fine-grained inclusions of rutile and, in garnet, rarely with clinopyroxene; together with coesite, garnet and omphacite represent the peak UHP mineral assemblage (Figs. 2a–2f). The barite forms rounded, anhedral grains (5–45 μm in diameter) without any sign of microcracks in the immediately adjacent host mineral, excluding the possibility of a later stage origin by fluid infiltration (cf. Rasmussen et al. 2011). Thus, we interpret these inclusions, as well as the rutile inclusions, to be primary *sensu* Roedder (1984) and Touret (2001), meaning they formed earlier than or synchronously with the growth of the host garnet and omphacite, most likely in the coesite stability field.

Barite in multiphase solid inclusions in the coesite and quartz eclogite

Type II barite occurs in rounded MSI in the outer parts of garnet and omphacite (Fig. 3a; and Fig. 4d in Wang et al. 2014), or in the central parts of these minerals as partially collapsed pucker structures associated with veinlets filled with epidote, biotite and K-feldspar that connect to phengite inclusions that have rims of biotite and epidote (Fig. 3b). The MSI range from tens to hundreds of microns across and mainly comprise the assemblage Brt + Bt + Ep ± Kfs ± Ab ± Zrn (Figs. 3a and 3b; and Fig. 4d from Wang et al. 2014). Barite is variable in the mode, from ~75 vol% to ~1 vol%. In addition to barite, MSI in garnet may contain both Ba-bearing K-feldspar and Ba-poor K-feldspar, and albite, and connect to inclusions of mica via cuspate K-feldspar–plagioclase veinlets (Fig. 4e in Wang et al. 2014). The MSI are also interpreted to be

primary inclusions, raising the possibility that the type I and type II barite could be partly contemporaneous.

Barite in multi-mineral pseudomorphs in the coesite and quartz elcogite

Type III barite occurs in regularly shaped multi-mineral pseudomorphs in garnet in both coesite and quartze clogite. The pseudomorphs comprise Kfs + Qz + Ab + Brt ± Bt (Figs. 3c–3f), with a barite mode of <1 vol%. The shape and location of these pseudomorphs suggest replacement of a precursor mineral such as phengite or coesite (c.f. Zeng et al. 2007). Based on the morphology and mineralogy of the pseudomorphs, phengite is inferred to be the more likely precursor mineral at Yangkou rather than coesite as suggested by Zeng et al. (2007) for surface samples from near the CCSD borehole. Thus, we interpret these multi-mineral pseudomorphs to have been phengite relics from the prograde evolution that were preserved as inclusions in garnet, whereas phengite is absent from the peak phase assemblage (Wang et al. 2014).

Barite aggregations associated with hornblende and albite symplectite in the quartz eclogite

Type IV barite forms irregular patches associated with hornblende and albite symplectite that partially replaced omphacite (Fig. 4). The edges of the barite against the symplectite are mutually embayed in a fashion that suggests replacement of one by the other, although the sequence is ambiguous. This barite is typically coarser than the other types, with patches ranging from tens to several hundreds of microns across that sometimes taper out along grain boundaries (yellow

arrows in Fig. 4c), suggesting these are pinched veinlets that formed along fluid-generated cracks. The barite exhibits irregular or patchy extinction in crossed polarized light (Fig. 4b). To investigate this feature, several representative patches of barite were analyzed using EBSD to obtain crystallographic orientation contrast images. The insets in Figs. 4e and 4f show the variable orientation of crystallographic domains within barite, suggesting that the individual barite patches are composed of multiple sub-grains.

Grain-boundary veinlets of barite in the quartz eclogite

Type V barite extends along grain boundaries between garnet, omphacite and quartz (Fig. 5). These grain-boundary veinlets are several microns in width and have no apparent interaction with garnet, omphacite or quartz (Figs. 5a and 5b). In places, the barite in the grain-boundary veinlets co-exists with small intergranular grains of barite (average diameter of ~35 μm; Figs. 5b and 5c). In addition, the barite veinlets form rings around concentrically zoned polymineralic aggregates (Fig. 5c) in a manner suggesting reaction, as indicated by the partially replaced pyrite in the core (Fig. 5d). From the innermost core to the outermost layer (Figs. 5c–5f), the mineralogy of these aggregates is pyrite, hematite, goethite and barite, respectively, as confirmed by Raman spectroscopy (Fig. 6). The hematite is commonly cut by goethite veinlets (Figs. 5d and 5f). Moreover, this mineral association is crosscut by K-feldspar veinlets (Figs. 5e and 5f).

BARITE CHEMISTRY

311 The SrO content for each type of barite (electronic Appendix I, Supplementary Table 1a; Fig.
312 7) is: type I, from below detection to 29.94 wt%; type II, 0.03–5.23 wt%; type III, 0.42–4.14
313 wt%; type IV, from below detection to 5.21 wt%, but predominantly < 2.5 wt%; and, type V,
314 from below detection to 2.85 wt%, but < 1.0 wt% except for 4 analyses. All show negative
315 correlations between BaO and SrO (Figs. 7a–7e), reflecting solid solution between barite and
316 celestine (Hanor 2000). Although the large dataset from Yangkou is dominated by barite with
317 concentrations of SrO < 5 wt%, the range of SrO concentrations is similar to those reported from
318 other locations within the Dabie–Sulu belt (Fig. 7f; data from Yang et al. 2006, 2010, and Zeng et
319 al. 2007; electronic Appendix I, Supplementary Table 1b). The type I barite compositions show a
320 negative correlation between BaO and SrO + CaO (Fig. 8a), and a marked increase in CaO
321 contents from < 2 wt% at SrO contents < 20 wt% to ~9 wt% at constant SrO of 17–25 wt% (Fig.
322 8b).
323

324 **WHOLE-ROCK TRACE ELEMENT CHEMISTRY**

325 At Yangkou there are transitional sequences preserved between incipiently metamorphosed
326 gabbro with relict magmatic texture and primary clinopyroxene and orthopyroxene to completely
327 recrystallized coesite-bearing eclogite (Zhang and Liou 1997). Therefore, the Yangkou outcrops
328 present an opportunity to compare geochemical characteristics among protolith metagabbro,
329 intergranular coesite-bearing UHP eclogite and country rock orthogneisses. The comparison may
330 shed light on the mobility of trace elements during continental subduction, particularly in relation
331 to the LILE.

To address this issue, in Fig. 9 we compare new whole-rock trace element data (Table 1) for two type I barite-bearing UHP eclogites (YK5-2a, YK24b) and three country rock orthogneisses (YK137-1, 16, 17), with published data for the metagabbros from Yang et al. (2014). The data are shown as primitive mantle normalized trace element and chondrite normalized rare earth element (REE) patterns in Figs. 9a and 9b.

It is evident that there are similarities and differences in trace element patterns between the barite-bearing eclogites and the metagabbros. When compared to the metagabbros, the barite-bearing eclogites are depleted in the LILE (Figs. 9a and 9c; Table 1), but both rock types exhibit similarly low high field strength element concentrations, such as Nb, Ta, Zr and Hf (Fig. 9d). Both rock types have flat chondrite normalized heavy rare earth element (HREE) patterns ($(Gd/Yb)_{cn}$ = 1.85–2.38), and negligible Eu anomalies ($(Eu/Eu^*)_{cn}$ = 0.96–1.07). However, the chondrite normalized light rare earth element (LREE) patterns for the eclogites are depleted with respect to the metagabbros and have shallower slopes (Figs. 9a and 9b; Table 1). The REE patterns are similar to those of metagabbros and eclogites reported by Chen et al. (2002) from Yangkou.

The trace element features of the country rock orthogneisses are similar to those of other granite gneisses in the Sulu belt (e.g., Zong et al. 2010; Xu et al. 2013). In the primitive mantle normalized trace element diagram (Fig. 9a), the orthogneisses are seen to be depleted in Ba, Nb, Ta and Sr, and enriched in Th, U, Pb, Zr and Hf. Orthogneisses have relatively flat chondrite normalized REE patterns ($(La/Sm)_{cn}$ = 2.45–3.30 and $(Gd/Yb)_{cn}$ = 0.71–1.23), with LREE concentrations lower than and HREE concentrations higher than the metagabbros, and

353 moderately negative Eu anomalies ($(Eu/Eu^*)_{cn}$ = 0.39–0.42; Fig. 9b). Concentrations of Ba and
354 Sr in the orthogneisses are similar to those of the barite-bearing eclogites, but are much lower
355 than concentrations in the metagabbros (Fig. 9c).
356
357 **Zr-IN-RUTILE THERMOMETRY**
358 The solubility of Zr in rutile is strongly temperature dependent. This feature may be used for
359 thermometry where the rutile co-exists with the appropriate buffer assemblage of zircon and a
360 SiO_2 polymorph (Zack et al. 2004; Watson et al. 2006; Ferry and Watson 2007; Tomkins et al.
361 2007). Zr-in-rutile thermometry has been applied previously to eclogites from the Dabie–Sulu
362 orogen (Gao C.G. et al. 2010; Zheng et al. 2011a; Gao X.Y. et al. 2014b).
363 In the UHP eclogite at Yangkou rutile occurs as either intergranular grains or as inclusions in
364 garnet and omphacite, ranging in size from several microns to tens of microns in diameter. The
365 rutiles do not show any visible alteration. Other inclusions in garnet and omphacite include type I
366 barite, sometimes in direct contact with rutile and, in garnet, clinopyroxene (Figs. 2e and 2f),
367 indicating synchronous crystallization and capture as primary inclusions. We note that rutile
368 inclusions in garnet from studies in other metamorphic belts are thought to preserve their primary
369 compositions (Zack et al. 2004). A SiO_2 polymorph is assumed present, based on the occurrence
370 of Coe/Qz in the samples, and zircon may occur as inclusions in the same grains with barite. In
371 the absence of zircon, Zr-in-rutile thermometry gives minimum temperatures (Zack et al. 2004).
372 The Zr concentration in the rutile inclusions varies from 40 to 324 ppm (see electronic
373 Appendix II, Supplementary Table 2). We consider analyses to be reliable if the concentration is

374 at and above a value equal to 3 times the detection limit, which was determined to be 20 ppm
375 (above). On this basis, 8 data have been excluded from the dataset used for the estimation of
376 temperature, which is based on 56 reliable analyses of Zr.

377 Zirconium-in-rutile temperatures were calculated using the pressure-dependent calibration of
378 Tomkins et al. (2007, their equation (10) for coesite stability), and assuming equilibrium is
379 maintained with co-existing zircon and coesite. As a representative example, the
380 zirconium-in-rutile temperatures are shown as a box plot at 3.5 GPa in Fig. 10a. We take the
381 upper edge of the box-plot box as a conservative estimate of temperature (e.g., $T = 679\ ^{o}C$ in Fig.
382 10a; Tomkins et al. 2007, p. 711), which yields a range from $T = 658 \pm 30\ ^{o}C$ at $P = 2.5$ GPa to T
383 $\approx 699 \pm 30\ ^{o}C$ at $P = 4.5$ GPa (additional box plots not shown; the range of temperatures is
384 shown as box 1 in Fig. 11a), where the $\pm 30\ ^{o}C$ uncertainty follows the recommendation of
385 Tomkins et al. (2007, p. 711).

386

387 **Ti-IN-ZIRCON THERMOMETRY**

388 The solubility of Ti in zircon is strongly temperature dependent. This feature may be used
389 for thermometry where the zircon co-exists with the appropriate buffer assemblage of a Ti-rich
390 mineral (rutile, titanite, ilmenite) and quartz (Watson and Harrison 2005; Watson et al. 2006;
391 Ferry and Watson 2007). Ti-in-zircon thermometry has been applied previously to eclogites from
392 the Dabie–Sulu orogen (Gao et al. 2011; Chen et al. 2012; Liu et al. 2012; Xu et al. 2012, 2013).

393 Zircon, as a main accessory mineral, is well developed in the eclogites at Yangkou. In one
394 amphibolite facies retrogressed eclogite analyzed by Wang et al. (2014) from General's Hill, a

few kilometers to the south of the Yangkou locality, zircon shows euhedral and prismatic shape with distinct core–rim structure in cathodoluminescence (CL). The zircon rims yielded a $^{206}Pb/^{238}U$ age of 224 ± 1.5 Ma (Supplementary Fig. 1a), which post-dates the peak of metamorphism of *ca*. 230 Ma (e.g., Liu and Liou 2011). Based on CL images (Fig. 7b from Wang et al. 2014), $^{206}Pb/^{238}U$ ages and REE patterns (Supplementary Figs. 1a and 1b), the zircon rims are metamorphic and are interpreted to record temperatures related to exhumation and retrogression (Rubatto 2002).

The Ti concentration in the zircon rims varies from 3 to 18 ppm (see in electronic Appendix III, Supplementary Table 3). Temperatures were calculated from these data using the calibration of Ferry and Watson (2007), which is calibrated at 1 GPa, assuming equilibrium is maintained with co-existing quartz and ilmenite (retrograde from rutile). Although quartz is a major mineral in the amphibolitic eclogite and a_{SiO2} is considered to have been 1, rutile has been retrograded to ilmenite and a_{TiO2} is taken to be 0.5 (Watson et al. 2006; Xu et al. 2012, 2013). The titanium-in-zircon temperatures are shown as a box plot in Fig. 10b (original data are in electronic Appendix III, Supplementary Table 3). As a conservative estimate of temperature we take the upper edge of the box-plot box, which yields T = 851 ± 20 ^{o}C (Fig. 10b). The ± 20 ^{o}C uncertainty follows the estimate of Ferry and Watson (2007, p. 434) that uncertainty on the calibration is up to ±16 ^{o}C according to temperature and our estimate that the analytical uncertainty on Ti measurements is unlikely to be more than ± 15 %. The calibration has a pressure dependence of approximately 50 ºC/GPa (Ferry and Watson 2007, p. 711), so that at 2 GPa, $T \approx$ 900 ± 20 ºC. In Fig. 11a the range of temperatures during decompression from 2 to 1

GPa is shown as box 5.

DISCUSSION

Although barite has been reported previously in UHP eclogite from the Sulu belt, the timing of crystallization and source of the fluid from which it precipitated remain uncertain. Arguments have been put forth for a prograde origin (Zeng et al. 2007; Yang et al. 2010), or a relationship to the peak UHP metamorphic stage (Ferrando et al. 2005), or an association with partial melting during decompression (Gao et al. 2012; Chen et al. 2014) or a link to fluid flow during exhumation (Sun et al. 2007; Yang et al. 2010). Because the occurrence of barite implies the presence of a high-salinity oxidizing fluid, melt, or supercritical fluid (Zhang et al. 2008; Frezzotti and Ferrando 2015; Tumiati et al. 2015), it is important to establish both the timing and origin of the barite found in UHP metamorphic rocks. This information is critical to the identification of fluid sources, particularly whether the fluid was internally buffered or not, determining the evolution of the fluid composition with changing *P–T* conditions, and assessing the geochemical behavior of Ba, Sr and S during continental subduction and exhumation.

In this study, we have identified five types of barite in the eclogite at Yangkou based on different microstructural settings. These are linked to: (1) the late prograde-to-peak metamorphic evolution (types I and II); (2) *in situ* melting of phengite during a high-pressure decompression stage (type III); and, (3) low-pressure amphibolite facies conditions, where barite patches (type IV) and veins (type V) in two distinct microstructural settings represent precipitation from an internally buffered aqueous fluid.

Barite inclusions in the cores of garnet and omphacite are associated with inclusions of rutile that yield temperatures of 658–699 °C at pressures of 2.5–4.5 GPa. This range of temperatures is significantly lower than the peak temperatures of > 800 to < 1000 °C calculated for the pressure range of 3.5–6.0 GPa (Wang et al. 2014). Therefore, we interpret the Zr-in-rutile temperatures to record part of the prograde evolution. We note that a similar interpretation was made by Zhang et al. (2009) for rutile inclusions in garnet and omphacite from core samples from the CCSD in the southern Sulu belt. Since rutile and type I barite are interpreted as primary inclusions and occur together, by implication the barite is coeval with rutile, and both were incorporated in garnet and omphacite during prograde growth (Fig. 11b). The presence of barite indicates that a high-salinity oxidizing fluid was available during the late prograde stage of the metamorphic evolution, most likely due to dehydration during subduction (Frezzotti and Ferrando 2015). Ultimately the garnet and omphacite equilibrated at the peak *P*–*T* conditions, which implies that barite can survive metamorphism at pressures that may have reached 7 GPa at temperatures up to 1000 °C (Ye et al. 2000; Wang et al. 2014). This confirms the remarkable stability of barite during metamorphism, as noted by Hanor (2000).

Although solid solution between barite and anhydrite has been experimentally confirmed as discontinuous and restricted, barite may accommodate minor amounts of Ca^{2+} (Hanor 2000 and references therein). In this study, higher Sr in the type I barite tends to be accompanied by higher Ca^{2+} (Fig. 8), suggesting that it is easier for Ca^{2+} to substitute for Sr^{2+} than Ba^{2+} because of their closer ionic radii. The wide range of SrO contents among the type I barite suggests that originally high SrO barite has been modified, perhaps by dehydration during progressive subduction

458 approaching the metamorphic peak and by H_2O exsolution from garnet and omphacite during
459 subsequent exhumation (Sheng et al. 2007). This interpretation is consistent with the occurrence
460 of variable high to low SrO barite in eclogites from further south in the Sulu belt in the vicinity
461 of the CCSD borehole, in which barite in pseudomorphs after coesite was interpreted to be relict
462 from the prograde stage (Zeng et al. 2007). In particular, we note the range of barite
463 compositions determined in the study by Zeng et al. (2007), where SrO varies from 34.65 wt% to
464 below detection, although only 4 of 21 analyses have SrO > 10 wt%. Zeng et al. (2007) attributed
465 this range in compositions to partial dissolution of barite by aqueous fluid and loss of Sr.
466 Preservation of the primary mineralogy in the metagabbros demonstrates either that
467 large-scale fluid migration did not occur or more likely that fluid flow was channelized, which
468 may indicate that the compositions of the metagabbros could be relatively unchanged from their
469 magmatic protoliths. These observations suggest to us that the attendant fluid during prograde
470 metamorphism was limited in quantity and probably internally buffered, consistent with
471 expectations both for the amount of aqueous fluid generated and lost during subduction, and the
472 expected source of these fluids in the crustal part of the subducting slab (van Keken et al. 2011;
473 Frezzotti and Ferrando 2015).
474 The Ba and Sr concentrations of eclogites and country rock orthogneisses are much lower
475 than concentrations of these elements in the metagabbros (Fig. 9c), which points to removal of
476 Ba and Sr. We postulate that the Ba and Sr were most likely removed by prograde dehydration
477 during subduction, via either an aqueous fluid or supercritical fluid (Zheng and Hermann 2014;
478 Frezzotti and Ferrando 2015). This interpretation is consistent with the inferred peak assemblage

in the UHP eclogite at Yangkou, which is essentially anhydrous, except for H_2O in nominally anhydrous minerals, and the expectation that subducting continental crust will lose most of its H_2O during prograde breakdown of hydrous minerals during subduction (van Keken et al. 2011). Furthermore, the experiments of Blount (1977) showed increased solubility of Ba and SO_4^{2-} in aqueous fluid with increasing pressure and salinity, which is consistent with prograde loss of LILEs. By contrast, removal of Ba and Sr during decompression and retrogression seems less prominent, given the evidence for only localized grain boundary fluid migration.

Type II barite occurs in the MSI, which are generally located towards the rims of the peak rock-forming minerals garnet and omphacite. We interpret these MSI to be primary inclusions of supercritical fluid trapped close to the metamorphic peak during growth of the host minerals (Fig. 11b; Roedder 1984; Touret 2001). A supercritical fluid exhibiting complete miscibility between aqueous fluid and hydrous melt is anticipated during the late prograde to peak evolution, since pressures exceeded the second critical endpoints for both felsic and mafic rock compositions (Manning 2004; Hermann et al. 2006; Hack et al. 2007). This is consistent with earlier studies on Ky quartzites and Ky–Ph–Ep eclogites (Ferrando et al. 2005) and metamorphic veins hosted in the UHP eclogites (Zhang et al. 2008) from the Donghai area in the southern Sulu belt that demonstrated the existence of an oxidizing supercritical fluid during peak metamorphism.

The parent supercritical fluid had a composition dominated by SiO_2, Al_2O_3, K_2O, Na_2O, CaO, FeO, MgO, SO_4^{2-}, BaO, SrO and ZrO_2 and is interpreted to be locally derived and in equilibrium with the host eclogite. The MSI vary from those with Ba-rich K-feldspar together with K-feldspar and albite, but without barite (Fig. 4e in Wang et al. 2014), to MSI with barite-bearing

mineral assemblages (Figs. 3a and 3b). In addition, type II barite shows a range of SrO compositions (Fig. 7b). These features suggest a gradual concentration of Ba in the supercritical fluid with entrapment occurring over a range of *P–T* conditions approaching the metamorphic peak (Fig. 11b). The supercritical fluid may have separated into immiscible hydrous silicate melt and aqueous fluid during decompression (Hermann et al. 2006; Hack et al. 2007; Zheng et al. 2011b), as suggested by the formation of pucker structures (Fig. 3b) and the occurrence of amphibolite facies hydrous minerals at the margins of the MSI and lining the cracks that radiate from these structures. Thus, we interpret the pucker structure and amphibolite facies hydrous minerals to be formed by decrepitation and crystallization at lower pressure during exhumation.

Based on petrographic analysis, Wang et al. (2014) argued that phengite was absent from the peak phase assemblage, forming as a matrix mineral during the early stage of decompression. The preservation of intragranular coesite in UHP eclogite at Yangkou and the absence of phengite at the metamorphic peak indicate that these rocks were locally fluid absent at the start of exhumation. The introduction of phengite into the metamorphic phase assemblage during the initial decompression is inferred to reflect exsolution of H_2O from the nominally anhydrous minerals, which may reach 2,500 ppm and 3,500 ppm in garnet and omphacite, respectively at UHP conditions (Katayama and Nakashima 2003; Xia et al. 2005; Katayama et al. 2006; Sheng et al. 2007; Chen et al. 2011; Gong et al. 2013).

Type III barite occurs in elongate multi-mineral pseudomorphs included in garnet that we interpret to be former prograde phengite, based on the lamellar habit and mineralogy (Figs. 3c and 3d). We interpret the replacement mineral assemblage in the pseudomorphs to have formed

during *in situ* melting of phengite (Fig. 11b). The cracks radiating from the pseudomorphs (Figs. 3c–3f) probably formed at this time. This interpretation is consistent with the inference from multiple studies in the Dabie–Sulu ogogen that melting induced by breakdown of phengite has occurred in the eclogites (e.g., Gao et al. 2012; Liu et al. 2013; Chen et al. 2014; Wang et al. 2014). In the absence of SrO contents in barite much above 5 wt% it is impossible to say whether any barite was relict as inclusions in the former phengite (cf. the study by Zeng et al. 2007). However, since phengite is the major carrier of LILEs in eclogite, the breakdown of phengite will liberate Ba and Sr to the melt (Zack et al. 2001; Hermann 2002; Hermann and Rubatto 2009). Therefore, we interpret the precipitation of the type III barite to record crossing the solidus at low pressure during cooling.

Type IV barite is preserved as aggregates of sub-grains associated with hornblende and albite symplectite. The sub-grain structure of this barite indicates precipitation from fluid and grain aggregation. During this process the eclogite was retrogressed with omphacite becoming partially replaced by hornblende and albite symplectites (Fig. 11b).

The aqueous fluid associated with type IV barite precipitation is likely to have been internally buffered, based on the following petrographic and geochemical evidence. (1) The retrogressed eclogite is associated with largely unretrogressed UHP eclogite that preserves abundant intergranular coesite, demonstrating that pervasive infiltration of an external fluid is unlikely to have occurred. (2) The retrograde symplectites of hornblende and albite after omphacite (and garnet) are not well developed and are limited to pinched veinlets that formed along fluid-generated cracks. (3) Earlier O and H isotope studies on UHP eclogite indicate that

542 the fluid in equilibrium with the UHP eclogite was internally buffered and showed no evidence
543 of infiltration from the country rock gneisses (Zhang et al. 2003; Zheng et al. 2003; Chen et al.
544 2007).

545 Type V barite occurs as thin veinlets that co-exist with intergranular grains of barite; these
546 veinlets are associated with a distinctive ring structure and replacement of pyrite by hematite and
547 goethite with barite at the edge. This microstructure is described for the first time from UHP
548 eclogite. Since both hematite and goethite indicate an oxidizing environment, and the
549 microstructure suggests the presence of a grain boundary fluid, we infer that pyrite has reacted
550 locally with a highly oxidizing fluid to transform into hematite and goethite. Inferred model
551 reactions are $4FeS_2 + 15O_2 + 8H_2O \rightarrow 4Fe_2O_3 + 8SO_4^{2-} + 16H^+$ (Fleming 2009) and $4FeS_2 +$
552 $15O_2 + 10H_2O \rightarrow 4FeO(OH) + 8SO_4^{2-} + 16H^+$ (Murad and Rojik 2005), which could also
553 include the reaction from hematite to goethite $Fe_2O_3 + H_2O \rightarrow 2FeO(OH)$ (Gualtieri and
554 Venturelli 1999). These oxidation reactions are inferred to supply enough SO_4^{2-} for growth of the
555 type V barite. The oxidizing fluid is likely locally derived aqueous fluid at amphibolite facies
556 conditions (Fig. 11b).

557 The type V barite is inferred to have precipitated from an internally generated fluid similar to
558 the type IV barite, based on the following observations. (1) Both types of barite occur in the
559 same samples, suggesting a close genetic relationship. (2) Both types of barite tend to occur
560 along grain boundaries (Figs. 4c and 6a–6c). (3) For both types, the SrO concentrations of barite
561 are dominated by low values, generally < 2.5 wt% (Figs. 7d and 7e). The solubility of Ba^{2+} and
562 SO_4^{2-} in the fluid will decrease with decreasing pressure and temperature (Blount 1977).

Therefore, we posit that the ongoing release of H_2O from garnet and omphacite, coupled with the continued breakdown of phengite and the decreasing solubility of Ba^{2+} and SO_4^{2-} during retrogression to the amphibolite facies promoted the sporadic precipitation of barite continuously from type IV to V (Fig. 11b).

IMPLICATIONS

Although the evolution of the fluid phase accompanying metamorphism in continental subduction zones is known to be important, our understanding of the origin, nature and behavior of the fluid during subduction and subsequent exhumation has recently taken on a new focus in relation to the exsolution of H_2O from nominally anhydrous minerals and the possibility of melting during decompression (e.g., Hermann et al. 2006; Hack et al. 2007; Zheng 2009; Zhang et al. 2011; Zheng et al. 2011b; Hermann and Rubatto 2014; Zheng and Hermann 2014; Frezotti and Ferrando 2015). Our study of the microstructural setting and chemistry of barite in the UHP eclogite at Yangkou in the central Sulu belt has further advanced our understanding of local fluid generation and migration.

In this study, we have argued that fluid-assisted precipitation of barite occurred during both the late prograde stage of subduction as well as during the subsequent exhumation of the crust from mantle depths back to normal depths, and we have interpreted successive episodes of barite precipitation to record fluid generation and migration at the grain scale. These processes result in the local redistribution of Ba, Sr and S during continental subduction and exhumation. Throughout the metamorphic evolution the attendant fluid phase was internally buffered and

584 highly oxidizing. Furthermore, we have explained the low Ba and Sr concentrations of the UHP
585 eclogite and associated country rock orthogneisses as a consequence of prograde fluid loss rather
586 than as a feature related to either decompression or late retrogression to amphibolite facies
587 mineralogy along grain boundaries in some eclogites.

588 In detail, we have shown that aqueous and supercritical fluids were available successively
589 during the prograde growth of garnet and omphacite, as recorded by inclusions of barite and MSI
590 in these minerals. We have proposed that after the metamorphic peak, during the early stage of
591 decompression, H_2O exsolved from garnet and omphacite migrated to and along grain
592 boundaries to promote growth of phengite. We explained the formation of multi-mineral
593 pseudomorphs containing barite by *in situ* melting of phengite inclusions in garnet during
594 decompression and subsequent crystallization on crossing the solidus at lower pressure. Finally,
595 we interpreted the occurrences of barite as irregular patches associated with hornblende and
596 albite symplectite and as veinlets associated with partial replacement of pyrite as due to
597 continued exsolution of H_2O from garnet and omphacite during ongoing decompression to
598 amphibolite facies. Thus, these features record fluid migration at the end of the decompression
599 stage of the exhumation.

600 The increase in modal barite from the late prograde stage to the retrograde amphibolite
601 facies stage may indicate an increase in the availability of local internally buffered fluid during
602 exhumation. We interpret the high Sr/Ba of some type I barite to be primary, but these
603 compositions have been partially modified subsequently to lower Sr/Ba during progressive
604 subduction and exhumation. By contrast, the later generations of barite consistently record low

Sr/Ba. We interpret this change to indicate that high Sr/Ba characterized the attendant fluid during late prograde metamorphism, whereas the metamorphic fluids generated approaching metamorphic peak and post-peak during decompression and exhumation were characterized by low Sr/Ba.

ACKNOWLEDGEMENTS

This study was financially supported by the National Natural Science Foundation (Nos. 41272225) and the Fundamental Research Funds for the Central Universities, China University of Geosciences (Wuhan) (No. CUG–G1323511572). We thank Haihong Chen for help with whole-rock trace element analysis, Mouchun He for help with Raman spectroscopy and Zhenyu Chen and Shuiyuan Yang for help with EPMA analysis. We acknowledge constructive reviews from Anonymous and Simona Ferrando, and editorial advice from Daniela Rubatto.

REFERENCES CITED

Auzanneau, E., Vielzeuf, D., and Schmidt, M.W. (2006) Experimental evidence of decompression melting during exhumation of subducted continental crust. Contributions to Mineralogy and Petrology, 152, 125–148.

Blount, C.W. (1977) Barite solubilities and thermodynamic quantities to 300 ^{o}C and 1400 kbars. American Mineralogist, 62, 942–957.

Brown, M. (2013) Granite: from genesis to emplacement. Geological Society of America Bulletin, 125, 1079–1113.

Brown, M., Korhonen, F.J., and Siddoway, C.S. (2011) Organizing melt flow through the crust. Elements, 7(4), 261–266.

Chang, L.L.Y., Howie, R.A., and Zussman, J. (1996) Rock-forming minerals, Volume 5B Second Edition. Non-silicates: Sulphates, Carbonates, Phosphates, Halides. Longman Group Limited, 383 pp.

Chen, B., Ye, K., and Liu, J.B. (2002) Cogenetic relationship of the Yangkou gabbro-to-granite unit, Su-Lu terrane, eastern China, and implications for UHP metamorphism. Journal of the Geological Society, 159(4), 457–467.

Chen, R.X., Zheng, Y.F., Gong, B., Zhao, Z.F., Gao, T.S., Chen, B., and Wu, Y.B. (2007) Origin of retrograde fluid in ultrahigh-pressure metamorphic rocks: constraints from mineral hydrogen isotope and water content changes in eclogite–gneiss transitions in the Sulu orogen. Geochimica et Cosmochimica Acta, 71(9), 2299–2325.

Chen, R.X., Zheng, Y.F., and Gong, B. (2011) Mineral hydrogen isotopes and water contents in ultrahigh-pressure metabasite and metagranite: constraints on fluid flow during continental subduction-zone metamorphism. Chemical Geology, 281, 103–124.

Chen, R.X., Zheng, Y.F., and Hu, Z.C. (2012) Episodic fluid action during exhumation of deeply subducted continental crust: Geochemical constraints from zoisite–quartz vein and host metabasite in the Dabie orogen. Lithos, 155, 146–166.

Chen, Y.X., Zheng, Y.F., Gao, X.Y., and Hu, Z.C. (2014) Multiphase solid inclusions in zoisite-bearing eclogite: evidence for partial melting of ultrahigh-pressure metamorphic rocks during continental collision. Lithos, 200, 1–21.

Coats, J.S., Smith, C.G., Fortey, N.J., Gallagher, M.J., May, F.,and McCourt, W.J. (1980) Strata-bound barium–zinc mineralization in Dalradian schist near Aberfeldy, Scotland. Transactions of the Institution of Mining and Metallurgy Section B – Applied Earth Science, 89, B110–B122.

Ernst, W., Tsujimori, T., Zhang, R., and Liou, J.G. (2007) Permo-Triassic collision, subduction-zone metamorphism, and tectonic exhumation along the East Asian continental margin. Annual Review of Earth and Planet Sciences, 35, 73–110.

Ferrando, S., Frezzotti, M.L., Dallai, L., and Compagnoni, R. (2005) Multiphase solid inclusions in UHP rocks (Su-Lu, China): Remnants of supercritical silicate-rich aqueous fluids released during continental subduction. Chemical Geology, 223, 68–81.

Ferrero, S., Wunder, B., Walczak, K., O'Brien, P.J., and Ziemann, M.A. (2015) Preserved near ultraghihpressure melt from continental crust subducted to mantle depths. Geology, http://dx.doi.org/10.1130/G36534.1.

Ferry, J.M., and Watson, E.B. (2007) New thermodynamic models and revised calibrations for the Ti-in-zircon and Zr-in-rutile thermometers. Contributions to Mineralogy and Petrology, 154(4), 429–437.

Fleming, C.A. (2009) Basic iron sulphate—a potential killer for pressure oxidation processing of refractory gold concentrates if not handled appropriately.Technical Bulletin, 6.

Fortey, N.J., Coats, J.S., Gallagher, M.J., Smith, C.G., and Greenwood, P.G. (1993) New strata-bound barite and base metals in Middle Dalradian Rocks near Braemar, Northeast Scotland. Transactions of the Institution of Mining and Metallurgy Section B – Applied Earth Science, 102, B55–B64.

Franz, L., Romer, R.L., Klemd, R., Schmid, R., Oberhansli, R., Wagner, T., and Dong, S.W. (2001) Eclogite-facies quartz veins within metabasites of the Dabie Shan (eastern China): pressure-temperature-time-deformation path, compostion of the fluid phase and fluid flow

during exhumation of high-pressure rocks. Contributions to Mineralogy and Petrology, 141(3), 322–346.

Frezzotti, M.L., and Ferrando, S. (2015) The chemical behavior of fluids released during deep subduction based on fluid inclusions. American Mineralogist, 100, 352–377.

Gao, C.G., Liu, Y.S., Zong, K.Q., Hu, Z.C., and Gao, S. (2010) Microgeochemistry of rutile and zircon in eclogites from the CCSD main hole: Implications for the fluid activity and thermo-history of the UHP metamorphism. Lithos, 115(1), 51–64.

Gao, X.Y., Zheng, Y.F., and Chen, Y.X. (2011) U–Pb ages and trace elements in metamorphic zircon and titanite from UHP eclogite in the Dabie orogen: constraints on *P–T–t* path. Journal of Metamorphic Geology, 29, 721–740.

Gao, X.Y., Zheng, Y.F., and Chen, Y.X. (2012) Dehydration melting of ultrahigh-pressure eclogite in the Dabie orogen: evidence from multiphase solid inclusions in garnet. Journal of Metamorphic Geology, 30, 193–212.

Gao, X.Y., Zheng, Y.F., Chen, Y.X., and Hu, Z. (2014a) Composite carbonate and silicate multiphase solid inclusions in metamorphic garnet from ultrahigh-P eclogite in the Dabie orogen. Journal of Metamorphic Geology, 32, 961–980.

Gao, X.Y., Zheng, Y.F., Xia, X.P., and Chen, Y.X. (2014b) U-Pb ages and trace elements of metamorphic rutile from ultrahigh-pressure quartzite in the Sulu orogen. Geochimica et Cosmochimica Acta, 143, 87–114.

Gong, B., Chen, R.X., Zheng, Y.F. (2013) Water contents and hydrogen isotopes in nominally anhydrous minerals from UHP metamorphic rocks in the Dabie–Sulu orogenic belt. Chinese Science Bulletin, 58, 4384–4389.

Gualtieri, A.F., and Venturelli, P. (1999) In situ study of the goethite-hematite phase transformation by real time synchrotron powder diffraction. American Mineralogist, 84, 895–904.

Guo, S., Ye, K., Chen, Y., Liu, J.B, Mao, Q., and Ma, Y.G. (2012) Fluid-rock interaction and element mobilization in UHP metabasalt: constraints from an omphacite-epidote vein and host eclogites in the Dabie orogen. Lithos, 136, 145–167.

Guo, S., Ye, K., Yang, Y.H., Chen, Y., Zhang, L.M., Liu, J.B., Mao, Q., and Ma, Y.G. (2014) In situ Sr isotopic analyses of epidote: tracing the sources of multi-stage fluids in ultrahigh-pressure eclogite (Ganghe, Dabie terrane). Contributions to Mineralogy and Petrology, 167(2), 1–23.

Hack, A.C., Thompson, A.B., and Aerts, M. (2007) Phase relations involving hydrous silicatemelts, aqueous fluids, and minerals. Reviews in Mineralogy and Geochemistry, 65, 129–185.

Hacker, B.R., Wallis, S.R., McWilliams, M.O., and Gans, P.B. (2009) $^{40}Ar/^{39}Ar$ Constraints on the tectonic history and architecture of the ultrahigh–pressure Sulu orogen. Journal of Metamorphic Geology, 27, 827–844.

Hanor, J.S. (2000) Barite–celestine geochemistry and environments of formation. Reviews in Mineralogy and Geochemistry, 40(1), 193–275.

Hermann, J. (2002) Allanite: thorium and light rare earth element carrier in subducted crust. Chemical Geology, 192(3–4), 289–306.

Hermann, J., and Rubatto, D. (2009) Accessory phase control on the trace element signature of sediment melts in subduction zones. Chemical Geology, 265(3), 512–526.

Hermann, J., and Rubatto, D. (2014) Subduction of continental crust to mantle depth: geochemistry of ultrahigh-pressure rocks. Treatise Geochem, 4, 309–340.

Hermann, J., Spandler, C., Hack, A., and Korsakov, A.V. (2006) Aqueous fluids and hydrous melts in high-pressure and ultra-high pressure rocks: Implications for element transfer in subduction zones. Lithos, 92, 399–417.

Hermann, J., Zheng, Y.F., and Rubatto, D. (2013) Deep Fluids in Subducted Continental Crust. Elements, 9, 281–287.

Hu, Z.C., Gao, S., Liu, Y.S., Hu, S.H., Chen, H.H., and Yuan, H.L. (2008) Signal enhancement in laser ablation ICP-MS by addition of nitrogen in the central channel gas. Journal of Analytical Atomic Spectrometry, 23, 1093–1101.

John, T., Klemd, R., Gao, J., and Garbe-Schonberg, C.D. (2008) Trace-element mobilization in slabs due to non steady-state fluid-rock interation: constraints from an eclogite-facies transport vein in blueschist (Tianshan, China). Lithos, 103, 1–24.

Katayama, I., Nakashima, S. (2003) Hydroxyl in clinopyroxene from the deep subducted crust: Evidence for H_2O transport into the mantle. American Mineralogist, 88, 229–234.

Katayama, I., Nakashima, S., and Yurimoto, H. (2006) Water content in natural eclogite and implication for water transport into the deep upper mantle. Lithos, 86, 245–259.

Kribek, B., Hladikova, J., Zak, K., Bendl, J., Pudilova, M., and Uhlik, Z. (1996) Barite–hylophane sulfide ores at Rozna, Bohemian Massif, Czech Republic: Metamorphosed black shale-hosted submarine exhaltive mineralization. Economic Geology, 91, 14–35.

Labrousse, L., Prouteau, G., and Ganzhorn, A.C. (2011) Continental exhumation triggered by partial melting at ultrahigh pressure. Geology, 39, 1171–1174.

Labrousse, L., Duretz, T.,and Gerya, T. (2015) H_2O-fluid-saturated melting of subducted continental crust facilitates exhumation of ultrahigh-pressure rocks in continental subduction zones. Earth and Planetary Science Letters, 428, 151–161.

Li, S.G., Xiao, Y.L., Liou, D.L., Chen, Y.Z., Ge, N.J., Zhang, Z.Q., Sun, S.S., Cong, B.L.,Zhang, R.Y., Hart, S.R., and Wang, S.S. (1993) Collision of the North China and Yangtse Blocks and formation of coesite-bearing eclogites: Timing and processes. Chemical Geology, 109, 89–111.

Li, X.P., Yan, J.Y., Schertl, H.P., Kong, F.M., and Xu, H. (2014) Eclogite from the Qianliyan Island in the Yellow Sea: a missing link between the mainland of China and the Korean peninsula. European Journal of Mineralogy, 2403.

Liou, J.G., and Zhang, R.Y. (1996) Occurrences of intergranular coesite in ultrahigh-P rocks from the Sulu region, eastern China: implications for lack of fluid during exhumation. American Mineralogist, 81, 1217–1221.

Liu, F.L., and Liu, P.H. (2009) U-Pb dating, trace element and Hf isotopic characteristics of zircons from meta-gabbro in Yangkou area, north Sulu UHP terrane. Acta Petrologica Sinica, 25(9), 2113–2131 (in Chinese with English abstract).

Liu, F.L., and Liou, J.G. (2011) Zircon as the best mineral for *P*–*T*–time history of UHP metamorphism: A review on mineral inclusions and U–Pb SHRIMP ages of zircons from the Dabie–Sulu UHP rocks. Journal of Asian Earth Sciences, 40, 1–39.

Liu, F.L., Robinson, P.T., and Liu, P.H. (2012) Multiple partial melting events in the Sulu UHP terrane: zircon U–Pb dating of granitic leucosomes within amphibolite and gneiss. Journal of Metamorphic Geology, 30, 887–906.

Liu, F.L., Xu, Z.Q., and Liou, J.G. (2004) Tracing the boundary between UHP and HP metamorphic belts in the southwestern Sulu terrane, eastern China: evidence from mineral inclusions in zircons from metamorphic rocks. International Geology Review, 46(5), 409–425.

Liu, J.B., Ye, K., Cong, B.L., and Fan, H.R. (2000) The barite and anhydrite inclusions in zircon of gneisses from ultrahigh pressure metamorphic zone of the Dabie Mountains and their implications. Acta Petrologica Sinica, 16(4), 482–484 (in Chinese with English abstract).

Liu, J.B., Ye, K., Maruyama, S., Cong, B.L., and Fan, H.R. (2001) Mineral inclusions in zircon from gneisses in the ultrahigh-pressure zone of the Dabie Mountains, China. The Journal of Geology, 109, 523–535.

Liu, Q., Hermann, J., and Zhang, J.F. (2013) Polyphase inclusions in the Shuanghe UHP eclogites formed by subsolidus transformation and incipient melting during exhumation of deeply subduced crust. Lithos, 177, 91–109.

Liu, Q., Jin Z.M., and Zhang J.F. (2009) An experimental study of dehydration melting of phengite-bearing eclogite at 1.5–3.0 GPa. Chinese Science Bulletin, 54, 2090–2100.

Liu, Y.S., Hu, Z.C., Gao, S., Günther, D., Xu, J., Gao, C.G., and Chen, H.H. (2008) *In situ* analysis of major and trace elements of anhydrous minerals by LA-ICP-MS without applying an internal standard. Chemical Geology, 257(1), 34–43.

Manning, C.E. (2004) The chemistry of subduction-zone fluids. Earth and Planetary Science Letters, 223, 1–16.

Martin, L. A.J., Hermann, J., Gauthiez-Putallaz, L., Whitney, D.L., Vitale Brovarone, A., Fornash, K.F., and Evans, N.J. (2014) Lawsonite geochemistry and stability – implication for trace element and water cycles in subduction zones. Journal of Metamorphic Geology, 32, 455–478.

Mibe, K., Kawamoto, T., Matsukage, K.N., Fei Y.W., and Ono, S. (2011) Slab melting versus slab dehydration in subduction-zone magmatism. Proceedings of the National Academy of Sciences, 108(20), 8177–8182.

Murad, E., and Rojik, P. (2005) Iron mineralogy of mine-drainage precipitates as environmental indicators: review of current concepts and a case study from the Sokolov Basin, Czech Republic. Clay Minerals, 40, 427–440.

Ni, J.L., Liu, J.L., Tang, X.L., Yang, H.B., Xia, Z.M., and Guo, Q.J. (2013) The Wulian Metamorphic Core Complex: A Newly Discovered Metamorphic Core Complex along the Sulu Orogenic Belt, Eastern China. Journal of Earth Science, 24(3), 297–313.

Philippot, P., and Selverstone, J. (1991) Trace-element-rich brines in eclogitic veins: Implications for fluid composition and transport during subduction. Contributions to Mineralogy and Petrology, 106, 417–430.

Philippot, P., Chevallier, P., Chopin, C., and Dubessy, J. (1995) Fluid composition and evolution in coesite-bearing rocks (Dora-Maira massif, Western Alps): Implications for element recycling during subduction. Contributions to Mineralogy and Petrology, 121, 29–44.

Rasmussen, B., Fletcher, I.R., Muhling, J.R., Gregory, Courtney, J., and Wilde, S.A. (2011). Metamorphic replacement of mineral inclusions in detrital zircon from Jack Hills, Australia: Implications for the Hadean Earth. Geology, 39, 1143–1146.

Roedder, E. (1984) Fluid Inclusions. Reviews in Mineralogy, 12, 678.

Rubatto, D. (2002) Zircon trace element geochemistry: partitioning with garnet and the link between U–Pb ages and metamorphism. Chemical Geology, 184, 123–138.

Sakamaki, K., and Ogasawara, Y. (2014) Hydroxyl in clinopyroxene and titanite in a UHP diamond-free garnet-clinopyroxene rock from the Kokchetav Massif, northern Kazakhstan. International Geology Review, 56, 133–149.

Scambelluri, M., and Philippot, P. (2001) Deep fluids in subduction zones. Lithos, 55, 213–227.

Sheng, Y.M., Xia, Q.K., Dallai, L., Yang, X.Z., and Hao, Y.T. (2007) H_2O contents and D/H ratios of nominally anhydrous minerals from ultrahigh-pressure eclogites of the Dabie orogen, eastern China. Geochimica et Cosmochimica Acta, 71, 2079–2103.

Sheng, Y.M., Zheng, Y.F., Li, S.N., and Hu, Z. (2013) Element mobility during continental collision: insights from polymineralic metamorphic vein within UHP eclogite in the Dabie orogen. Journal of Metamorphic Geology, 31, 221–241.

Sizova, E., Gerya, T., and Brown, M. (2012) Exhumation mechanisms of melt-bearing ultrahigh pressure crustal rocks during collision of spontaneously moving plates. Journal of Metamorphic Geology, 30, 927–955.

Spandler, C., and Hermann, J. (2006) High-pressure veins in eclogite from New Caledonia and their significance for fluid migration in subduction zones. Lithos, 89, 135–153.

Spandler, C., Pettke, T., and Rubatto, D. (2011) Internal and External Fluid Sources for Eclogite-facies Veins in the Monviso Meta-ophiolite, Western Alps: Implications for Fluid Flow in Subduction Zones. Journal of Petrology, 52(6), 1207–1236.

Sun, S.S., and McDonough, W.F. (1989) Chemical and isotopic systematics of oceanic basalts: implications for mantle composition and processes. Geological Society, London, Special Publications, 42(1), 313–345.

Sun, X.M., Tang, Q., Sun, W.D., Xu, L., Zhai, W., Liang, J.L., Liang, Y.H., Shen, K., Zhang, Z.M., Zhou, B., and Wang, F.Y. (2007) Monazite, iron oxide and barite exsolutions in apatite aggregates from CCSD drillhole eclogites and their geological implications. Geochimica et Cosmochimica Acta, 71, 2896–2905.

Tomkins, H.S., Powell, R., and Ellis, D.J. (2007) The pressure dependence of the zirconium-in-rutile thermometer. Journal of Metamorphic Geology, 25(6), 703–713.

Touret, J.L.R. (2001) Fluids in metamorphic rocks. Lithos, 55, 1–25.

Tumiati, S., Godard, G., Martin, S., Malaspina, N., and Poli, S. (2015) Ultra-oxidized rocks in subduction melanges? Decoupling between oxygen fugacity and oxygen availability in a Mn-rich metasomatic environment. Lithos, 226, 116–130.

van Keken, P.E., Hacker, B.R., Syracuse, E.M., and Abers, G.A. (2011) Subduction factory: 4. Depth-dependent flux of H_2O from subducting slabs worldwide. Journal of Geophysical Research–Solid Earth, 116, B01401.

Vitale Brovarone, A., Alard, O., Beyssac, O., Martin, L., and Picatto, M. (2014a) Lawsonite metasomatism and trace element recycling in subduction zones. Journal of Metamorphic Geology, 32, 489–514.

Vitale Brovarone, A., and Beyssac, O. (2014b) Lawsonite metasomatism: A new route for water to the deep Earth. Earth and Planetary Science Letters, 393, 275–284.

Wallis, S.R., Ishiwatari, A., Hirajima, T., Ye, K., Guo, J., Nakamura, D., Kato, T., Zhai, M., Enami, M., and Cong, B. (1997) Occurrence and field relationships of ultrahigh-pressure metagranitoid and coesite eclogite in the Su-Lu terrane, eastern China. Journal of the Geological Society, 154(1), 45–54.

Wallis, S., Tsuboi, M., Suzuki, K., Fanning, M., Jiang, L., and Tanaka, T. (2005) Role of partial melting in the evolution of the Sulu (eastern China) ultrahigh-pressure terrane. Geology, 33(2), 129–132.

Wang, L., Kusky, T., and Li, S.Z. (2010) Structural geometry and evolution of an exhumed ultra-high pressure eclogite massif, Yangkou Bay, Sulu Belt. Journal of Structural Geology, 32, 423–444.

Wang, L., Kusky, T., Polat, A., Wang, S.J., Jiang, X.F., Zong, K.Q., Wang, J.P., Deng, H., and Fu, J.M. (2014) Partial melting of deeply subducted eclogite from the Sulu Orogen in China. Nature Communications, 5:5604, DOI: 10.1038/ncomms6604 |www.nature.com/naturecommunications.

Watson, E.B., and Harrison T.M. (2005) Zircon thermometer reveals minimum melting conditions on earliest Earth. Science, 308, 841–844.

Watson, E.B., Wark, D.A., and Thomas, J.B. (2006) Crystallization thermometers for zircon and rutile. Contributions to Mineralogy and Petrology, 151(4), 413–433.

Whitney, D.L., and Evans, B.W. (2010) Abbreviations for names of rock-forming minerals. American mineralogist, 95(1), 185–187.

Wu, T.Y., and Fu, Y.T. (2014) Cretaceous deepwater lacustrine dedimentary sequences from the northernmost South China Block, Qingdao, China. Journal of Earth Science, 25(2), 241–251.

Xia, Q.K., Sheng, Y.M., Yang, X.Z., and Yu, H.M. (2005) Heterogeneity of water in garnets from UHP eclogites, eastern Dabieshan, China. Chemical Geology, 224, 237–246.

Xu, H.J., Ye, K., and Zhang, J.F. (2012) Temperature of Prograde Metamorphism, Decompressional Partial Melting and Subsequent Melt Fractional Crystallization in the

Weihai Migmatitic Gneisses, Sulu UHP Terrane: Constraints from Ti-in-Zircon Thermometer. Journal of Earth Sciences, 23(6), 813–827.

Xu, H.J., Ye, K., Song, Y.R., Chen, Y., Zhang, J.F., Liu, Q., and Guo, S. (2013) Prograde metamorphism, decompressional partial melting and subsequent melt fractional crystallization in the Weihai migmatitic gneisses, Sulu UHP terrane, eastern China. Chemical Geology, 341, 16–37.

Xu, Z.Q., Zeng, L.S., Liu, F.L., Yang, J.S., Zhang, Z.M., McWilliams, M., and Liou, J.G. (2006) Polyphase subduction and exhumation of the Sulu high-pressure-ultrahigh-pressure metamorphic terrane. Geological Society of America Special Papers, 403, 93–113.

Yakymchuk, C., and Brown, M. (2014) Consequences of open system melting in tectonics. Journal of the Geological Society, London, 171, 21–40.

Yakymchuk, C., Brown, M., Ivanic, T.J., and Korhonen, F.J. (2013) Leucosome distribution in migmatitic paragneisses and orthogneisses: A record of self-organized melt migration and entrapment in a heterogeneous partially-molten crust. Tectonophysics, 603, 136–154.

Yang, H., Zhang, L.F., and Liu, F.L. (2006) Barite-bearing UHP eclogite from the main borehole core of the Chinese Continental Scientific Drilling. Acta Geologica Sinica, 80, 1892–1897 (in Chinese with English abstract).

Yang, H., Zhang, L.F., and Liu, F.L. (2010) Study on barite as an accessory mineral in eclogite from main borehole core of the Chinese Continental Scientific Drilling (CCSD). Acta Petrologica Sinica, 26(7), 2073–2082 (in Chinese with English abstract).

Yang, J.J., Fan, Z.F., Yu, C., and Yan, R. (2014) Coseismic formation of eclogite facies cataclasite dykes at Yangkou in the Chinese Su-Lu UHP metamorphic belt. Journal of Metamorphic Geology, 32, 937–960.

Yao, Y.P., Ye, K., Liu, J.B., Cong, B.L., and Wang, Q.C. (2000) A transitional eclogite- to high pressure granulaite-facies overprint on coesite-eclogite at Taohang in the Sulu ultrahigh-pressure terrane, Eastern China. Lithos, 52(1), 109–120.

Yardley, B., Gleeson, S., Bruce, S., and Banks, D. (2000) Orogin of retrograde fluids in metamorphic rocks. Journal of Geochemical Exploration, 69–70, 281–285.

Ye, K., Hirajima, T., and Ishiwatari, A. (1996) The discovery of intergranular coesite in eclogite of Yangkou, Qingdao and its significance. Chinese Science Bulletin, 41(15), 1407–1408.

Ye, K., Cong, B.L., and Ye, D.N. (2000) The possible subduction of continental material to depths greater than 200 km. Nature, 407(6805), 734–736.

Zack, T., Moraes, R., and Kronz, A. (2004) Temperature dependence of Zr in rutile: empirical calibration of a rutile thermometer. Contributions to Mineralogy and Petrology, 148(4), 471–488.

Zack, T., Rivers, T., and Foley, S.F. (2001) Cs–Rb–Ba systematics in phengite and amphibole: an assessment of fluid mobility at 2.0 GPa in eclogites from Trescolmen, Central Alps. Contributions to Mineralogy and Petrology, 140, 651–669.

Zeng, L.S., Liu, F.L., Liang, F.H., and Chen, F.Y. (2007) Barite in omphacite-hosted K-feldspar + quartz polycrystalline aggregates from the Sulu eclogites and its implications. Chinese Science Bulletin, 52(21), 2995–3001.

Zhang, R.Y., and Liou, J.G. (1997) Partial transformation of gabbro to coesite-bearing eclogite from Yangkou, the Sulu terrane, eastern China. Journal of Metamorphic Geology, 15(2), 183–202.

Zhang, R.Y., Hirajima, T., Banno, S., Cong, B.L., and Liou, J.G. (1995) Petrology of ultrahigh-pressure rocks from the southern Su-Lu region, eastern China. Journal of Metamorphic Geology, 13(6), 659–675.

Zhang, R.Y., Iizuka, Y., Ernst, W.G., Liou, J.G., Xu, Z.Q., Tsujimori, T., Lo, C.H., and Jahn, B.M. (2009) Metamorphic P–T conditions and thermal structure of Chinese Continental Scientific Drilling main hole eclogites: Fe-Mg partitioning thermometer vs. Zr-in-rutile thermometer. Journal of Metamorphic Geology, 27,757–772.

Zhang, R.Y., Liou, J.G., Zheng, Y.F., and Fu, B. (2003) Transition of UHP eclogites to gneissic rocks of low-amphibolite facies during exhumation: evidence from the Dabie terrane, central China. Lithos, 70(3), 269–291.

Zhang, Z.M., Shen, K., Liou, J.G., Dong, X., Wang, W., Yu, F., and Liu, F. (2011) Fluid-rock interactions during UHP metamorphism: A review of the Dabie-Sulu orogen, east-central China. Journal of Asian Earth Sciences, 42(3), 316–329.

Zhang, Z.M., Shen, K., Sun, W.D., Liu, Y.S., Liou, J.G., Shi, C., and Wang, J.L. (2008) Fluids in deeply subducted continental crust: petrology, mineral chemistry and fluid inclusion of UHP metamorphic veins from the Sulu orogen, eastern China. Geochimica et Cosmochimica Acta, 72(13), 3200–3228.

Zheng, Y.F. (2009) Fluid regime in continental subduction zones: petrological insights from ultrahigh-pressure metamorphic rocks. Journal of the Geological Society, 166(4), 763–782.

Zheng, Y.F., and Hermann, J. (2014) Geochemistry of continental subduction-zone fluids. Earth, Planets and Space, 66(1), 93.

Zheng, Y.F., Fu, B., Gong, B., and Li, L. (2003) Stable isotope geochemistry of ultrahigh pressure metamorphic rocks from the Dabie–Sulu orogen in China: implications for geodynamics and fluid regime. Earth-Science Reviews, 62, 105–161.

Zheng, Y.F., Gao, T.S., Wu, Y.B., Gong, B., and Liu, X.M. (2007) Fluid flow during exhumation of deeply subducted continental crust: zircon U-Pb age and O-isotope studies of a quartz vein within ultrahigh-pressure eclogite. Journal of Metamorphic Geology, 25, 267–283.

Zheng, Y.F., Gao, X.Y., Chen, R.X., and Gao, T.S. (2011a) Zr-in-rutile thermometry of eclogite in the Dabie orogen: Constraints on rutile growth during continental subduction-zone metamorphism. Journal of Asian Earth Sciences, 40(2), 427–451.

Zheng, Y.F., Xia, Q.X., Chen, R.X., and Gao, X.Y. (2011b) Partial melting, fluid supercriticality and element mobility in ultrahigh-pressure metamorphic rocks during continental collision. Earth-Science Reviews, 107(3), 342–374.

Zong, K.Q., Liu, Y.S., Hu, Z.C., Kusky, T., Wang, D.B., Gao, C.G., Gao, S., and Wang, J.Q. (2010) Melting-induced fluid flow during exhumation of gneisses of the Sulu ultrahigh-pressure terrane. Lithos, 120(3), 490–510.

951 **Figure Captions**

952 **FIGURE 1.** (**a)** Location of the Sulu belt in China**.** NCC, North China Craton; TM, Tarim
953 Craton; YC, Yangtze Craton; CP, Cathaysia Plate. **(b**) A geological sketch map of the Sulu belt
954 (after Yao et al. 2000; Zong et al. 2010). WQF, Wulian–Qingdao Fault; JXF, Jiashan–Xiangshui
955 Fault; MF, Mishan Fault; WRF, Wendeng–Rongcheng Fault. (c) Geological map of Yangkou Bay
956 in the central Sulu belt, Eastern China (after Wang et al. 2010), showing major litho-tectonic
957 units and sample locations (eclogite – black stars, country rock orthogneiss – blue stars).
958
959 **FIGURE 2.** BSE images of type I barite located in the cores of garnet and omphacite; barite
960 preserves equant anhedral shapes without any surrounding cracks in the host minerals, and abuts
961 against rutile and clinopyroxene inclusions indicating synchronous overgrowth by the host
962 minerals. Mineral names are abbreviated according to the recommendations of Whitney and
963 Evans (2010).
964
965 **FIGURE 3.** BSE images of type II and type III barite. (**a**) Type II barite in multiphase solid
966 inclusions (MSI) located towards the rims of garnet and omphacite (see insert), or (**b**) in the
967 cores of these minerals as partially collapsed pucker structures (see insert) associated with
968 veinlets; (**c**–**f**) Type III barite in multi-mineral pseudomorphs (MMP) that have regular shapes
969 suggestive of precursor mineral such as phengite, (**d)** and (**f**) are enlargements of the areas
970 outlined in (**c)** and (**e**), respectively. Mineral names are abbreviated according to the
971 recommendations of Whitney and Evans (2010).

FIGURE 4. Photomicrographs, BSE images and crystal orientation contrast images of type IV barite. (**a, b**) Plane polarized and cross polarized light images of barite surrounded by hornblende and albite symplectite with mutually embayed margins; (**c, d**) BSE images of barite surrounded by hornblende and albite symplectites, barite tapers out along the grain boundary (yellow arrows at top left and lower parts of (**c**)); (**e, f**) Representative type IV barite (in area outlined) and crystal orientation contrast images (inset) showing variable crystal orientations. Mineral names are abbreviated according to the recommendations of Whitney and Evans (2010).

FIGURE 5. BSE images of type V barite and associated minerals. (**a**–**c**) Barite veinlets and co-existing intergranular barite along grain boundaries of garnet, omphacite and quartz; the inset figure in **c** is the Raman spectra referring to the analyzed spot shown in red; (**d**) Concentric mineral microstructure with relict pyrite in the core, hematite in the mantle, and goethite and barite at the rim; (**e, f**) K-feldspar veinlet crosscuts the barite, hematite, goethite and pyrite replacement structure, (**f)** is an enlargement of the area outlined in (**e)**. Mineral names are abbreviated according to the recommendations of Whitney and Evans (2010).

FIGURE 6. Typical Raman spectra of minerals associated with the Type V barite. (**a)** shows the core mineral in **Fig. 5(d)** is pyrite with major peaks at 343 and 377 cm^{-1}, and a minor peak at 436 cm^{-1}; (**b)** shows the mantle mineral in **Fig. 5(d)** is hematite with characteristic peaks at 218, 287, 402 and 658 cm^{-1}; (**c)** shows the rim mineral in **Fig. 5(d)** is goethite with characteristic peaks at

213, 294, 396, 550 and 597 cm^{-1}; and (**d)** shows the mineral at the outer edge in **Fig. 5(d)** is barite with characteristic peaks at459 and 985 cm^{-1}.

FIGURE 7. Covariation diagrams between BaO and SrO for (**a**–**e**) all five morphological types of barite in the UHP eclogite from Yangkou, and (**f**) barite in eclogites from other locations in the Sulu belt. Note the different scales in (**a**–**f**).

FIGURE 8. Covariation diagrams (**a**) between BaO and SrO + CaO, and (**b**) SrO and CaO for the type I barite in the UHP eclogite from Yangkou.

FIGURE 9. (**a**) Primitive mantle normalized trace element patterns, (**b**) chondrite-normalized rare earth element patterns, (**c**) whole-rock Ba–Sr concentrations of barite-bearing eclogites, country rock gneisses and protolith metagabbros, and (**d**) high field strength element concentrations for barite-bearing eclogites and protolith metagabbros. Normalization values are from Sun and McDonough (1989), whole-rock trace element data of one UHP barite-bearing eclogite (YK5-2a) is from Wang et al. (2014), trace element data of metagabbros are from Yang et al. (2014). Note the different scales in (**c**) and (**d**).

FIGURE 10. Box and whisker plots displaying the distribution of temperatures calculated by Zr-in-rutile thermometry at 3.5 GPa (**a**) and Ti-in-zircon thermometry at 1 GPa (**b**). The box represents the interquartile range (the middle 50 % of the data from the 25^{th} to the 75^{th} percentile),

the whiskers extend to 1.5 times the interquartile range in (**a**) and the open circle in (**a**) represents a suspected outlier, whereas the whiskers in (**b**) only extend to the limits of the data. The numbers beneath each box represent the number of data in each case. The temperature at the top of the box is shown in each case.

FIGURE 11. (**a**) *P–T* path for the UHP eclogite at Yangkou in the central Sulu belt (modified from Wang et al. 2014) and (**b**) the different types of barite in relation to the *P–T* evolution. Box 1 shows the Zr-in-rutile temperatures (with an uncertainty of ± 30 ºC) calculated at pressures from 2.5 to 4.5 GPa, box 2 shows the range of peak Grt–Cpx temperatures calculated at pressures > 3.5 GPa for the Coe eclogite (from Wang et al. 2014, supplementary data set 3), box 3 shows the *P–T* range for the Grt + Omp + Ph + Coe/Qz assemblage (from Wang et al. 2014, supplementary data set 3, with uncertainty assessed as ± 50 ºC and ± 0.2 GPa), line 4 shows the range of Grt–Cpx temperatures at 2.5 GPa for the Qz eclogite (from Wang et al. 2014, supplementary data set 3, with uncertainty assessed as ± 50 ºC), and box 5 shows the Ti-in-zircon temperatures (with an uncertainty of ± 20 ºC) calculated at pressures of 2 to 1 GPa for the retrogressed eclogite. The second critical endpoint for the basalt–water system (A) is from Mibe et al. (2011), and the grey box (B) shows the phase transition from Cpx + Ph + Qz to Bt + Pl + Grt + Melt from Auzanneau et al. (2006). Further explanation is given in the text. Mineral names are abbreviated according to the recommendations of Whitney and Evans (2010).

1033 **TABLE 1.** Trace element contents [ppm] of Barite-bearing Eclogites, Country orthogneisses and protolith Metagabbros.

1034 Values for metagabbro are from from Yang et al. (2014). Further explanation in text.

Lithology	Brt-bearing Eclogites		Country Gneisses			Metagabbros			
MMC	Grt+Omp+Coe/Qz+Brt		Qz+Ph+Pl+Assessory Minerals			Yang et al. 2014			
Sam. No.	YK5-2a	YK24b	YK137-1	YK137-16	YK137-17	07YK07	11YK01	11YK02	11YK05
Ga	19.40	20.20	19.60	19.00	19.30	*n.a.*	*n.a.*	*n.a.*	*n.a.*
Rb	1.71	2.34	62.20	36.70	60.90	37.50	24.50	34.30	21.10
Sr	68.30	81.20	30.10	72.00	24.80	818.00	834.00	890.00	593.00
Y	23.30	23.60	36.90	43.10	30.30	18.00	19.60	21.30	22.30
Zr	94.70	98.80	229.00	324.00	245.00	70.00	129.00	118.00	122.00
Nb	4.54	4.00	11.80	11.20	12.40	6.03	6.16	5.50	6.57
Sn	0.87	0.98	2.13	1.70	2.26	*n.a.*	*n.a.*	*n.a.*	*n.a.*
Cs	0.04	0.04	0.41	0.26	0.40	*n.a.*	*n.a.*	*n.a.*	*n.a.*
Ba	105.00	326.00	264.00	280.00	281.00	1152.00	1763.00	1670.00	459.00
La	12.10	13.60	18.00	36.40	14.70	31.20	41.60	42.80	38.10
Ce	26.70	30.70	53.50	85.60	47.20	60.90	77.60	80.90	76.70
Pr	3.48	4.03	5.61	9.17	4.55	7.25	9.46	9.76	9.40
Nd	15.00	17.00	20.40	33.20	16.50	29.40	36.20	36.70	37.10
Sm	3.45	3.71	4.61	7.14	3.88	5.83	7.42	7.02	7.06
Eu	1.23	1.27	0.57	0.89	0.52	1.74	2.22	2.09	2.17
Gd	4.31	4.44	4.20	6.60	3.67	5.24	5.48	5.49	6.59
Tb	0.78	0.77	0.78	1.16	0.68	0.67	0.74	0.80	0.91
Dy	4.36	4.38	5.29	7.17	4.47	3.32	3.66	4.13	4.60
Ho	0.83	0.82	1.21	1.50	0.98	0.70	0.77	0.82	0.97
Er	2.24	2.24	4.03	4.44	3.22	1.95	2.21	2.27	2.71
Tm	0.30	0.30	0.69	0.68	0.52	0.29	0.31	0.32	0.39
Yb	1.84	1.99	4.87	4.44	3.61	1.82	1.97	2.05	2.51
Lu	0.26	0.27	0.82	0.64	0.57	0.28	0.30	0.32	0.39
Hf	2.35	2.47	6.71	8.50	7.06	1.71	2.78	2.78	2.97
Ta	0.68	0.45	0.96	1.06	0.95	0.53	0.41	0.33	0.40
Tl	0.02	0.01	0.12	0.13	0.09	*n.a.*	*n.a.*	*n.a.*	*n.a.*
Pb	2.66	3.60	2.69	4.77	2.62	*n.a.*	*n.a.*	*n.a.*	*n.a.*
Th	1.26	1.63	11.30	11.90	13.50	5.43	5.11	3.19	6.46
U	0.24	0.24	2.18	2.64	2.25	0.74	0.97	0.61	2.02
Sr/Ba	0.65	0.25	0.00	0.26	0.09	0.71	0.47	0.53	1.29
∑LREE	61.96	70.31	102.69	172.40	87.35	136.32	174.50	179.27	170.53
∑REE	76.88	85.52	124.58	199.03	105.07	150.59	189.94	195.47	189.60
$(La/Sm)_{cn}$	2.38	2.27	2.52	3.30	2.45	3.46	3.62	3.94	3.49
$(Gd/Yb)_{cn}$	1.85	1.94	0.71	1.23	0.84	2.38	2.30	2.22	2.17

$(Eu/Eu^*)_{cn}$	0.96	0.98	0.39	0.40	0.42	0.96	1.07	1.03	0.97

Note: MMC represents main mineral composition; Sam. No. represents Sample number; normalization values from Sun and McDonough (1989). "*n.a.*" represents data not analyzed in original paper.

1035

Fig. 1

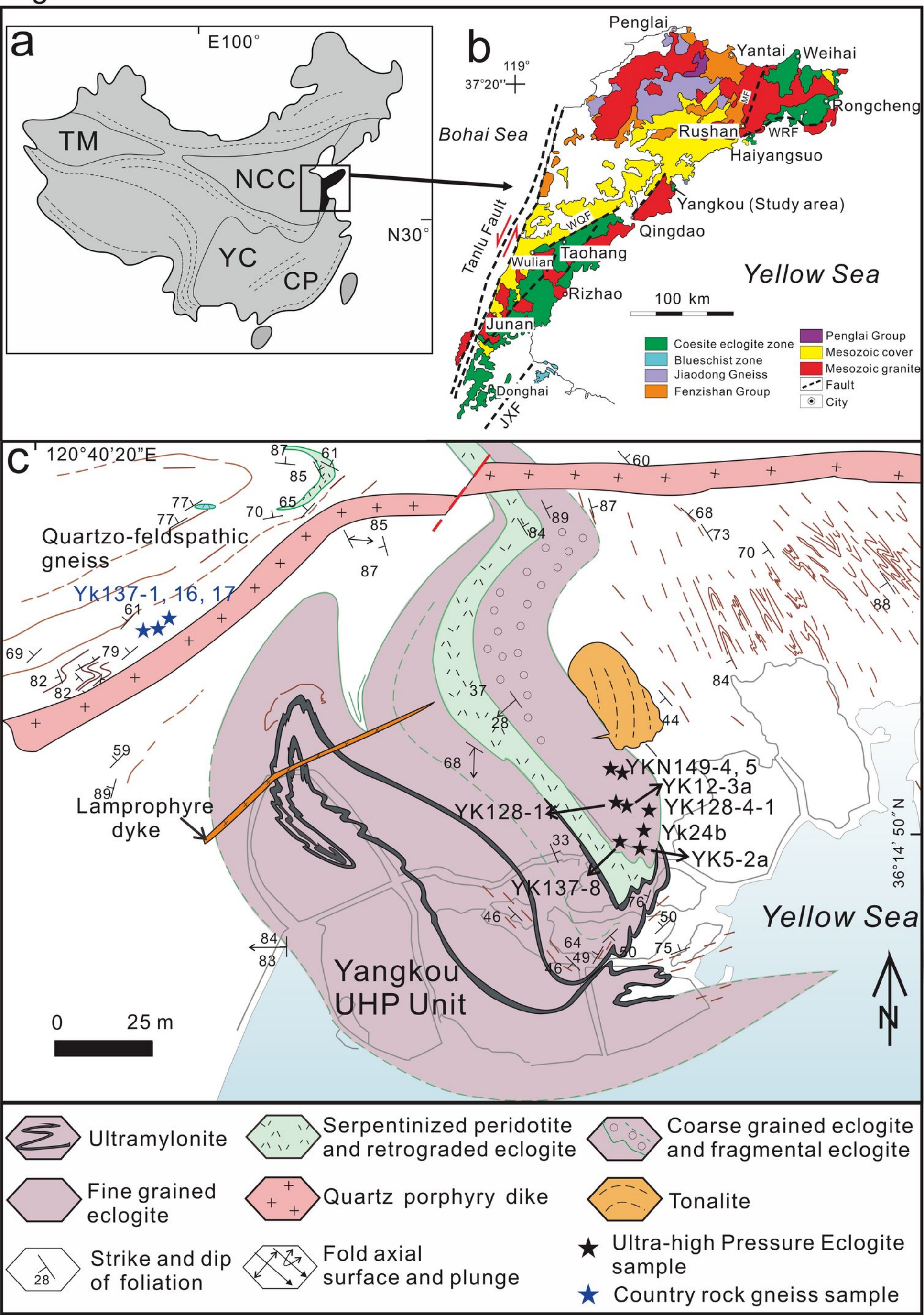
a
E100°
N30°
TM
NCC
YC
CP
b
119°
37°20''
Penglai
Yantai
Weihai
Rongcheng
Bohai Sea
MF
WRF
Rushan
Haiyangsuo
Yangkou (Study area)
Tanlu Fault
WQF
Qingdao
Taohang
Wulian
Yellow Sea
Rizhao
100 km
Junan
Donghai
JXF
Coesite eclogite zone
Blueschist zone
Jiaodong Gneiss
Fenzishan Group
Penglai Group
Mesozoic cover
Mesozoic granite
Fault
City
c
120°40'20"E
Quartzo-feldspathic gneiss
Yk137-1, 16, 17
Lamprophyre dyke
YKN149-4, 5
YK12-3a
YK128-1
YK128-4-1
Yk24b
YK5-2a
YK137-8
Yangkou UHP Unit
Yellow Sea
36°14' 50"N
0
25 m
N
Ultramylonite
Fine grained eclogite
Strike and dip of foliation
Serpentinized peridotite and retrograded eclogite
Quartz porphyry dike
Fold axial surface and plunge
Coarse grained eclogite and fragmental eclogite
Tonalite
Ultra-high Pressure Eclogite sample
Country rock gneiss sample

Fig. 2

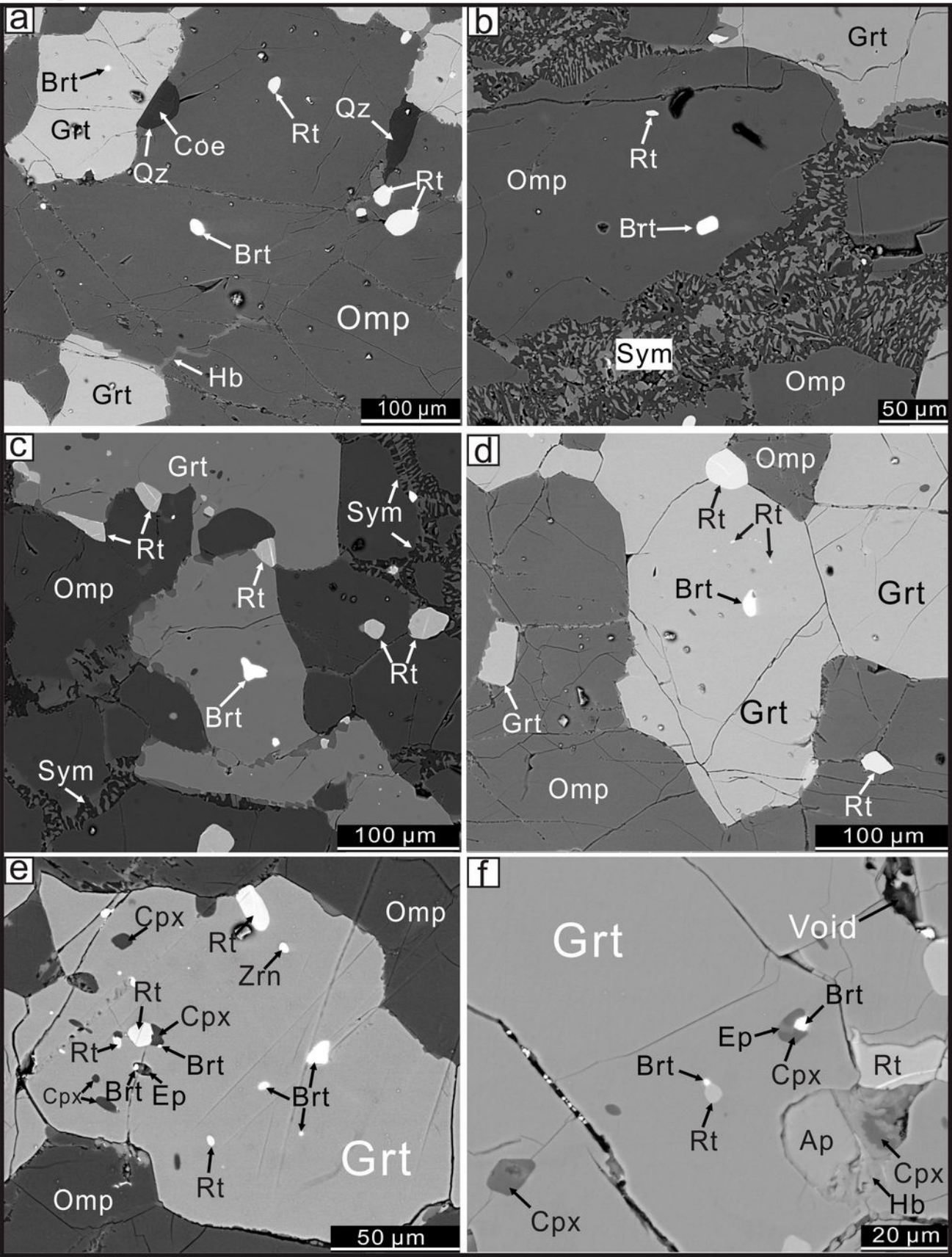
a
Brt
Grt
Coe
Qz
Rt
Qz
Rt
Brt
Omp
Hb
Grt
100 μm
b
Grt
Rt
Omp
Brt
Sym
Omp
50 μm
c
Grt
Rt
Sym
Omp
Rt
Rt
Brt
Sym
100 μm
d
Omp
Rt
Rt
Brt
Grt
Grt
Grt
Omp
Rt
100 μm
e
Cpx
Rt
Omp
Zrn
Rt
Cpx
Rt
Brt
Cpx
Brt
Ep
Brt
Grt
Rt
Omp
50 μm
f
Grt
Void
Brt
Ep
Cpx
Brt
Rt
Rt
Ap
Cpx
Hb
Cpx
20 μm

Fig. 3

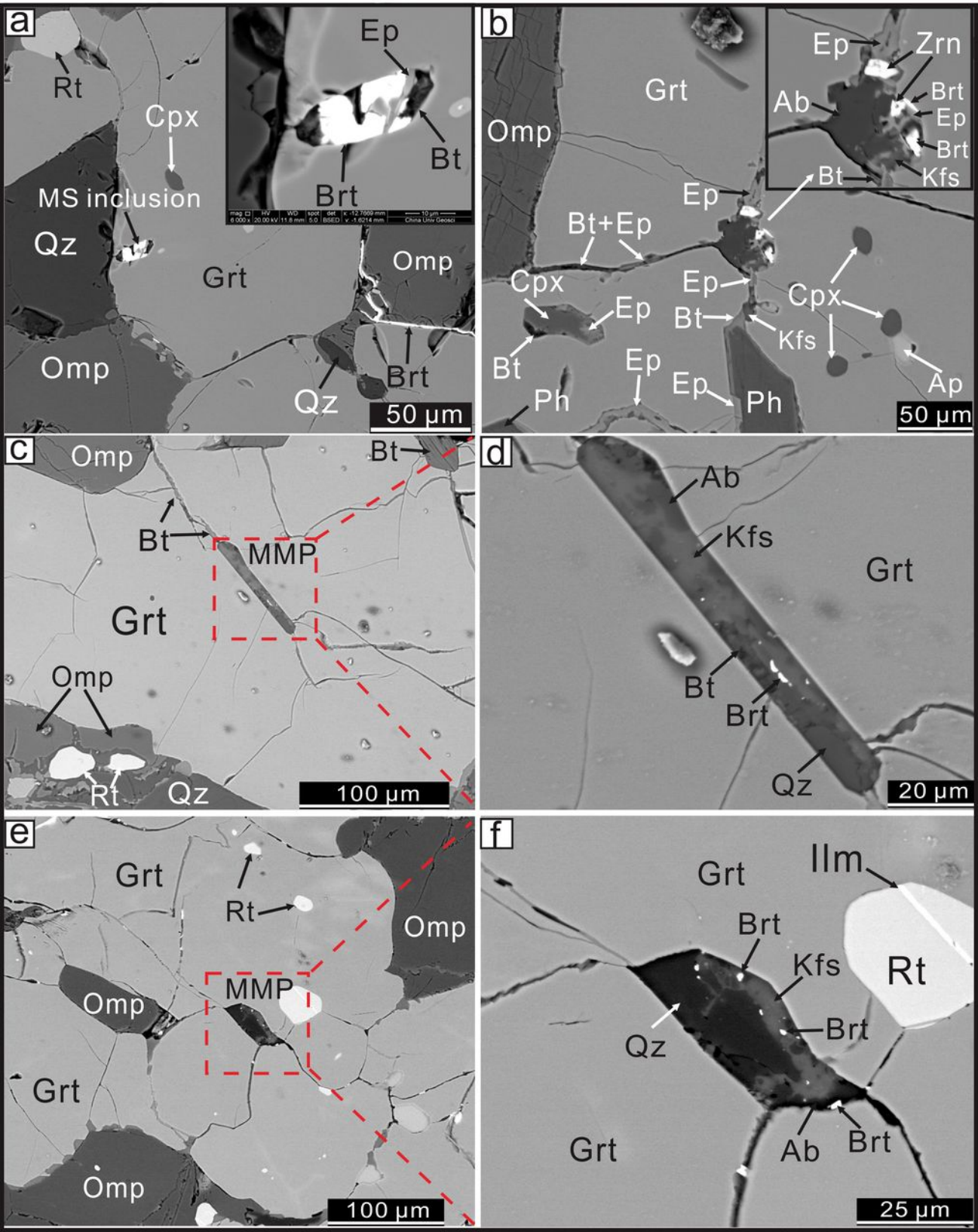
a
Rt
Cpx
MS inclusion
Qz
Grt
Omp
Omp
Qz
Brt
50 μm
Ep
Bt
Brt
b
Grt
Omp
Ep
Zrn
Brt
Ab
Ep
Brt
Bt
Kfs
Ep
Bt+Ep
Cpx
Ep
Ep
Cpx
Bt
Kfs
Bt
Ep
Ep
Ap
Ph
Ph
50 μm
c
Omp
Bt
Bt
MMP
Grt
Omp
Rt
Qz
100 μm
d
Ab
Kfs
Grt
Bt
Brt
Qz
20 μm
e
Grt
Rt
Omp
MMP
Omp
Grt
Omp
100 μm
f
Grt
Ilm
Brt
Kfs
Rt
Qz
Brt
Grt
Ab
Brt
25 μm

Fig. 4

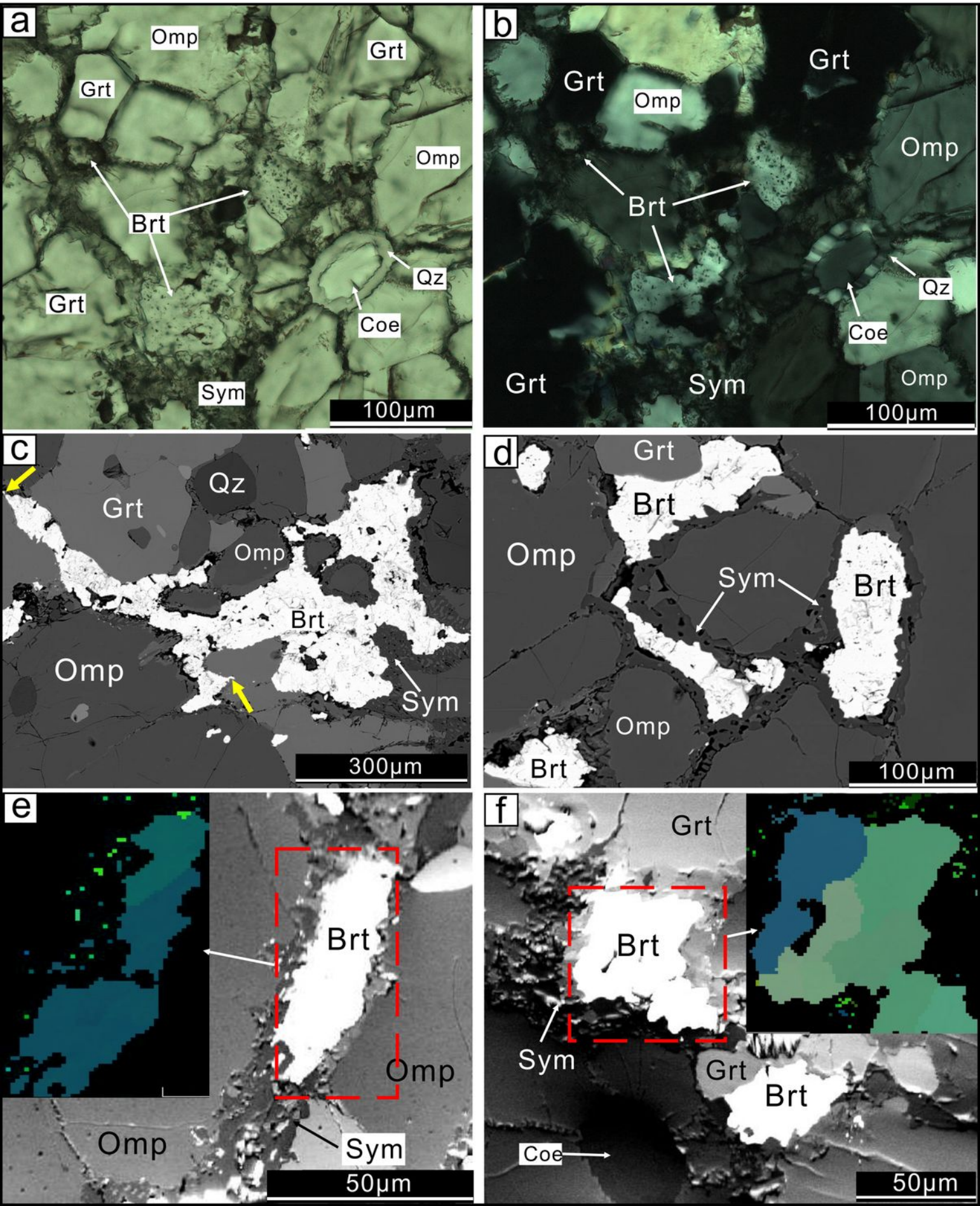
a
Omp
Grt
Grt
Omp
Brt
Qz
Grt
Coe
Sym
100μm
b
Grt
Grt
Omp
Omp
Brt
Qz
Coe
Grt
Sym
Omp
100μm
c
Qz
Grt
Omp
Brt
Omp
Sym
300μm
d
Grt
Brt
Omp
Sym
Brt
Omp
Brt
100μm
e
Brt
Omp
Omp
Sym
50μm
f
Grt
Brt
Sym
Grt
Brt
Coe
50μm

Fig. 5

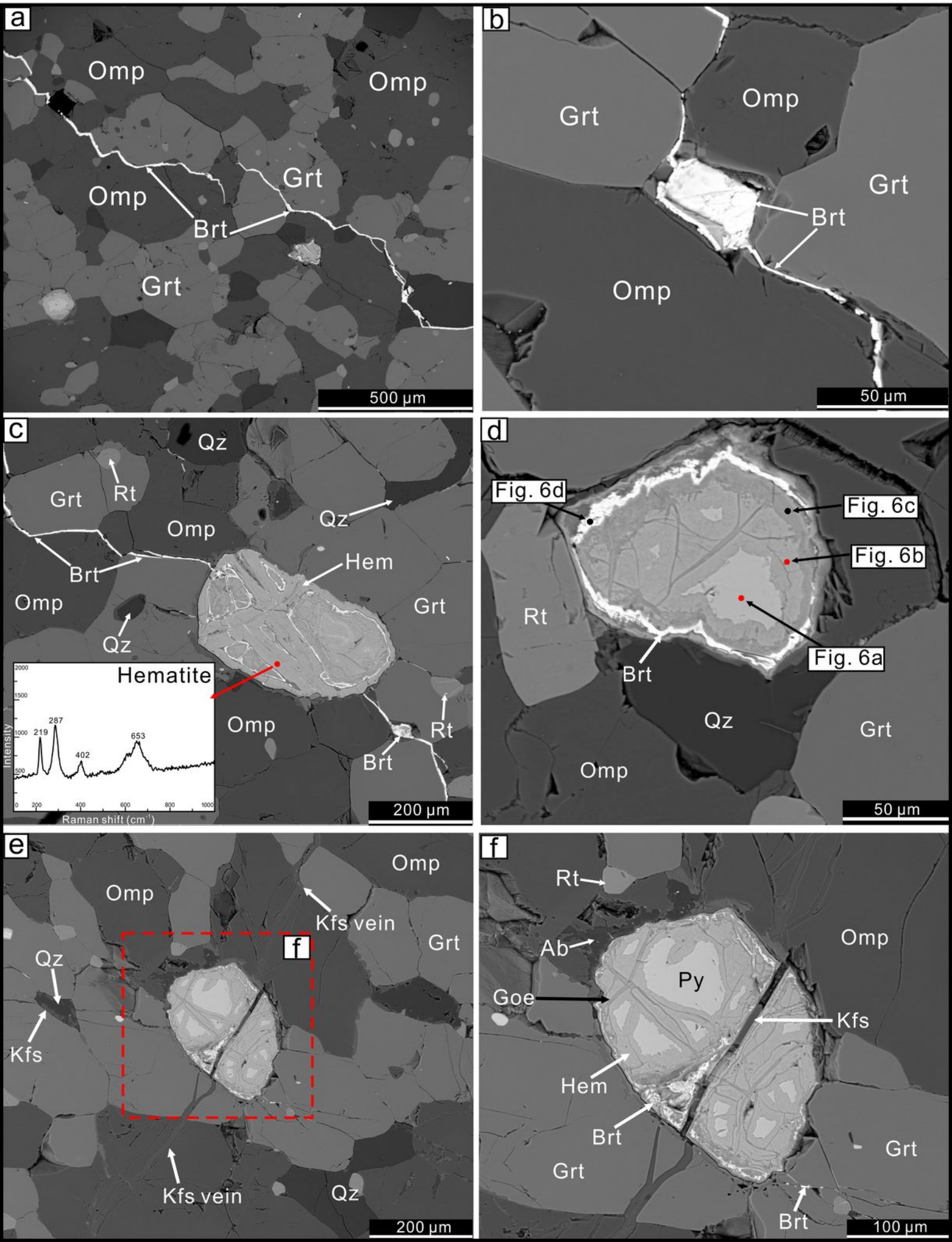
a
Omp
Omp
Grt
Omp
Brt
Grt
500 μm
b
Grt
Omp
Grt
Brt
Omp
50 μm
c
Qz
Grt
Rt
Qz
Omp
Hem
Brt
Omp
Grt
Qz
Hematite
Intensity
Raman shift (cm⁻¹)
Omp
Rt
Brt
200 μm
d
Fig. 6d
Fig. 6c
Fig. 6b
Fig. 6a
Rt
Brt
Qz
Grt
Omp
50 μm
e
Omp
Omp
Kfs vein
Grt
f
Qz
Kfs
Kfs vein
Qz
200 μm
f
Rt
Ab
Omp
Py
Goe
Kfs
Hem
Brt
Grt
Grt
Brt
100 μm

Fig. 6

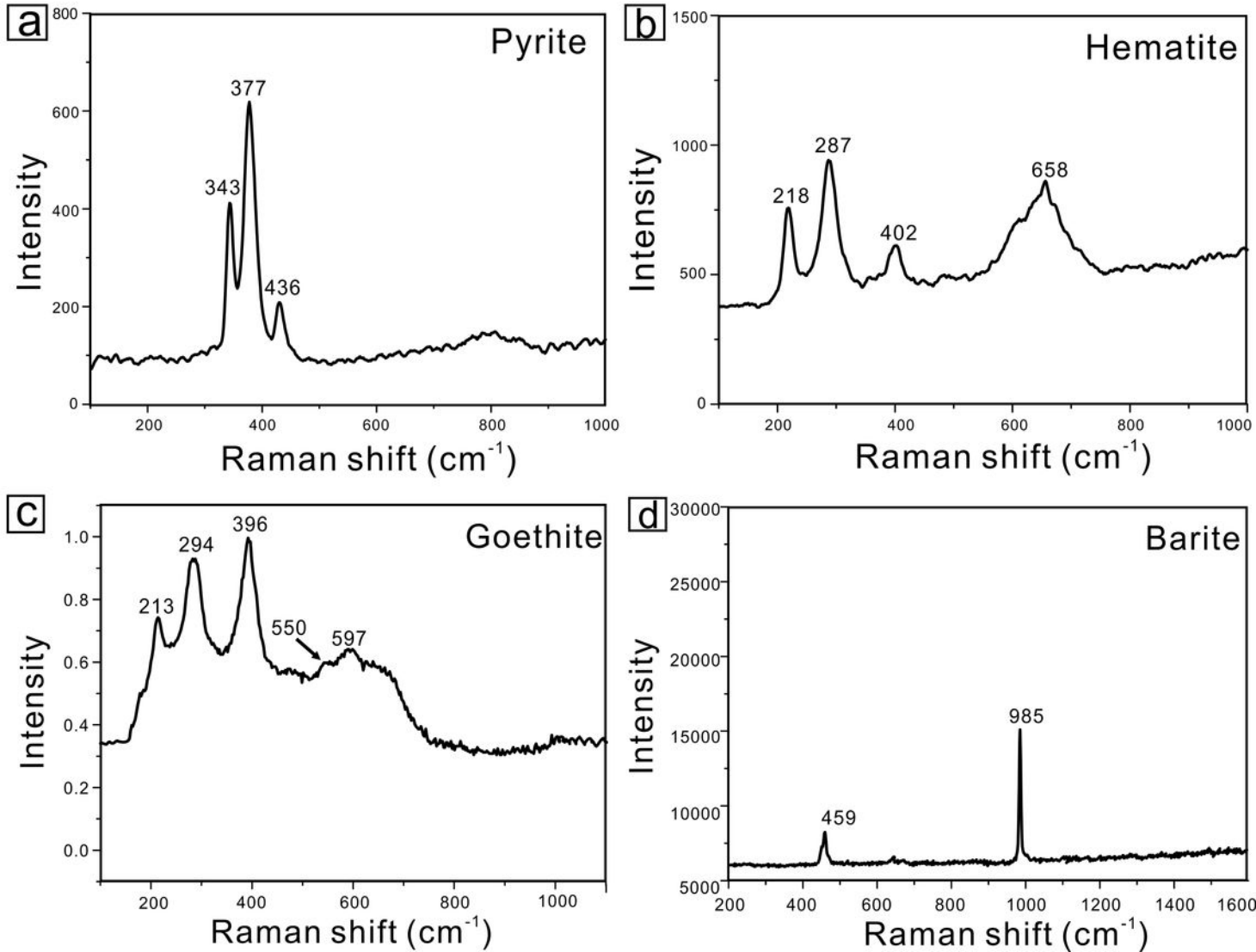
a
Pyrite
377
343
436
Intensity
Raman shift (cm-1)
b
Hematite
287
218
402
658
Intensity
Raman shift (cm-1)
c
Goethite
396
294
213
550
597
Intensity
Raman shift (cm-1)
d
Barite
985
459
Intensity
Raman shift (cm-1)

Fig. 7

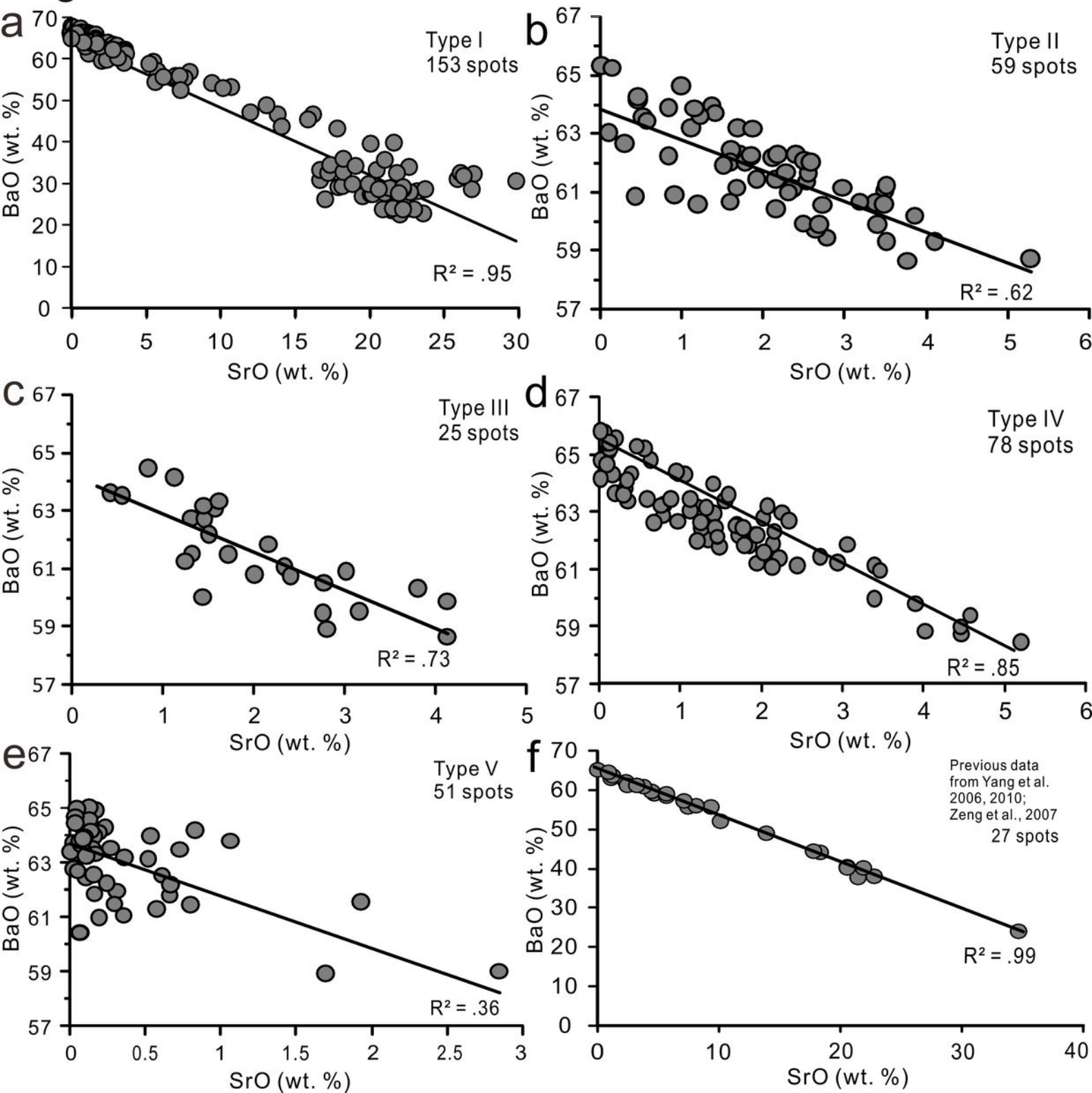
a
Type I
153 spots
R² = .95
BaO (wt. %)
SrO (wt. %)
b
Type II
59 spots
R² = .62
BaO (wt. %)
SrO (wt. %)
c
Type III
25 spots
R² = .73
BaO (wt. %)
SrO (wt. %)
d
Type IV
78 spots
R² = .85
BaO (wt. %)
SrO (wt. %)
e
Type V
51 spots
R² = .36
BaO (wt. %)
SrO (wt. %)
f
Previous data
from Yang et al.
2006, 2010;
Zeng et al., 2007
27 spots
R² = .99
BaO (wt. %)
SrO (wt. %)

Fig. 8

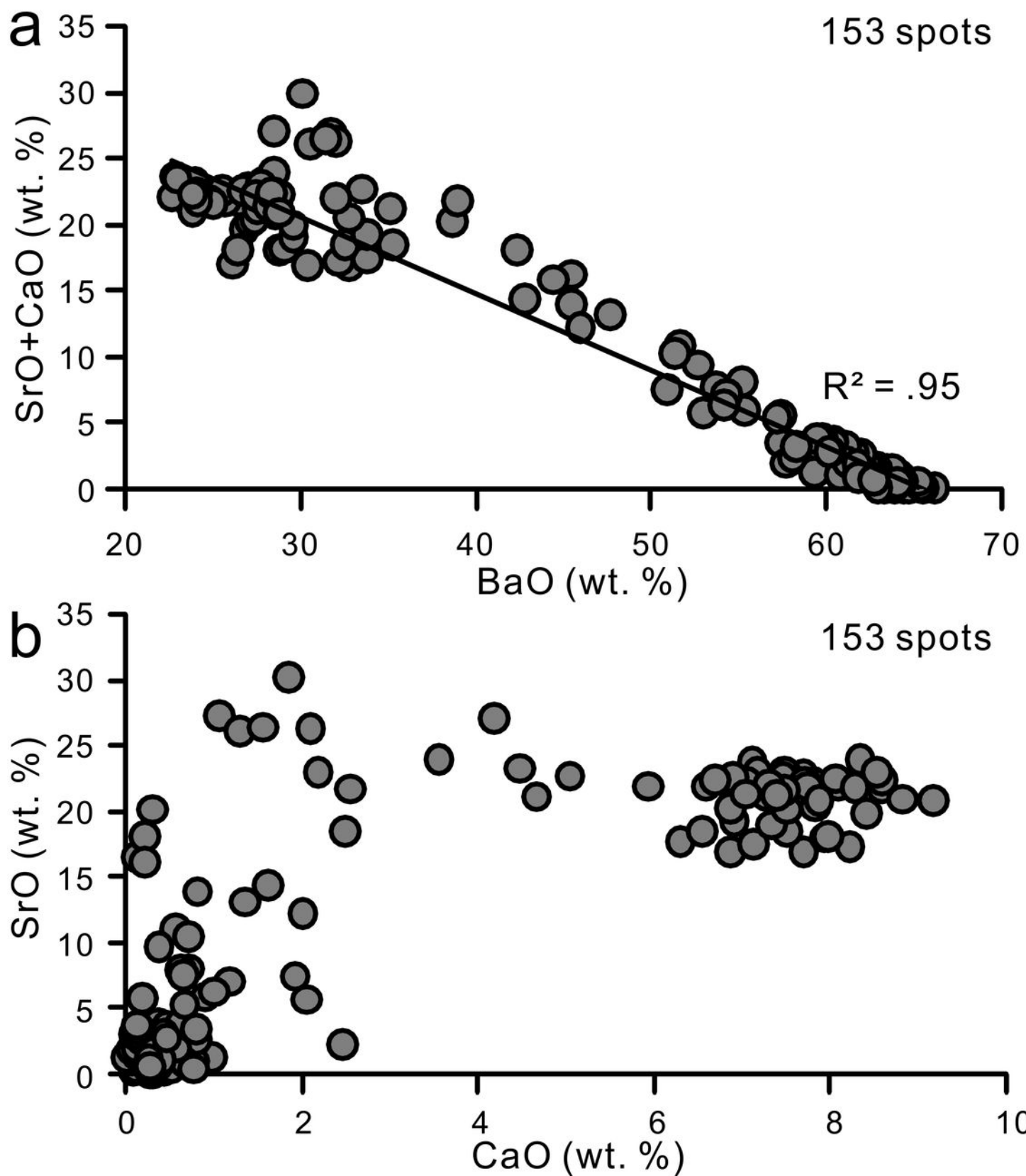

Fig. 9

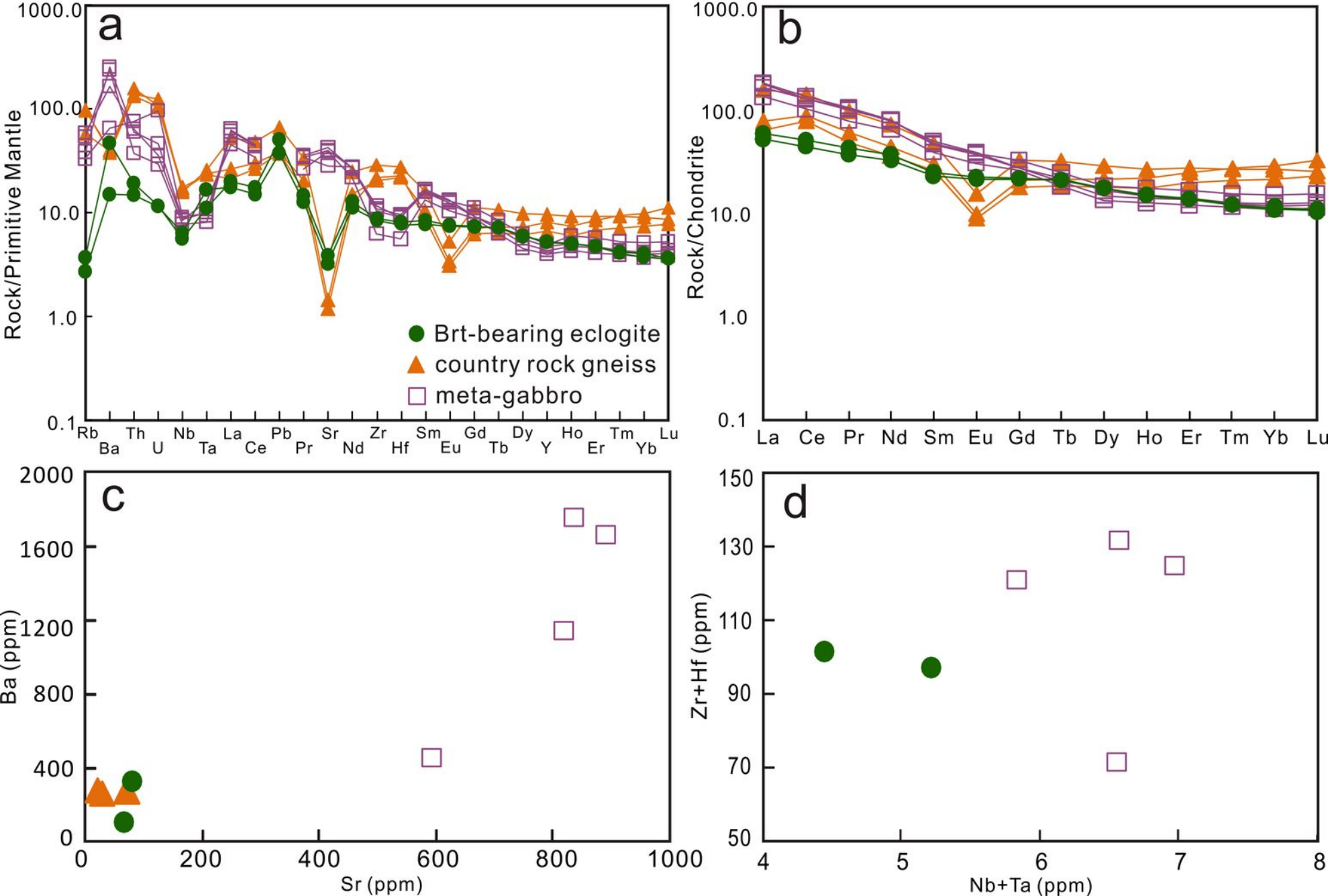
a
1000.0
100.0
10.0
1.0
0.1
Rock/Primitive Mantle
Rb Ba Th U Nb Ta La Ce Pb Pr Sr Nd Zr Hf Sm Eu Gd Tb Dy Y Ho Er Tm Yb Lu
Brt-bearing eclogite
country rock gneiss
meta-gabbro
b
1000.0
100.0
10.0
1.0
0.1
Rock/Chondrite
La Ce Pr Nd Sm Eu Gd Tb Dy Ho Er Tm Yb Lu
c
2000
1600
1200
800
400
0
Ba (ppm)
0 200 400 600 800 1000
Sr (ppm)
d
150
130
110
90
70
50
Zr+Hf (ppm)
4 5 6 7 8
Nb+Ta (ppm)

Fig. 10

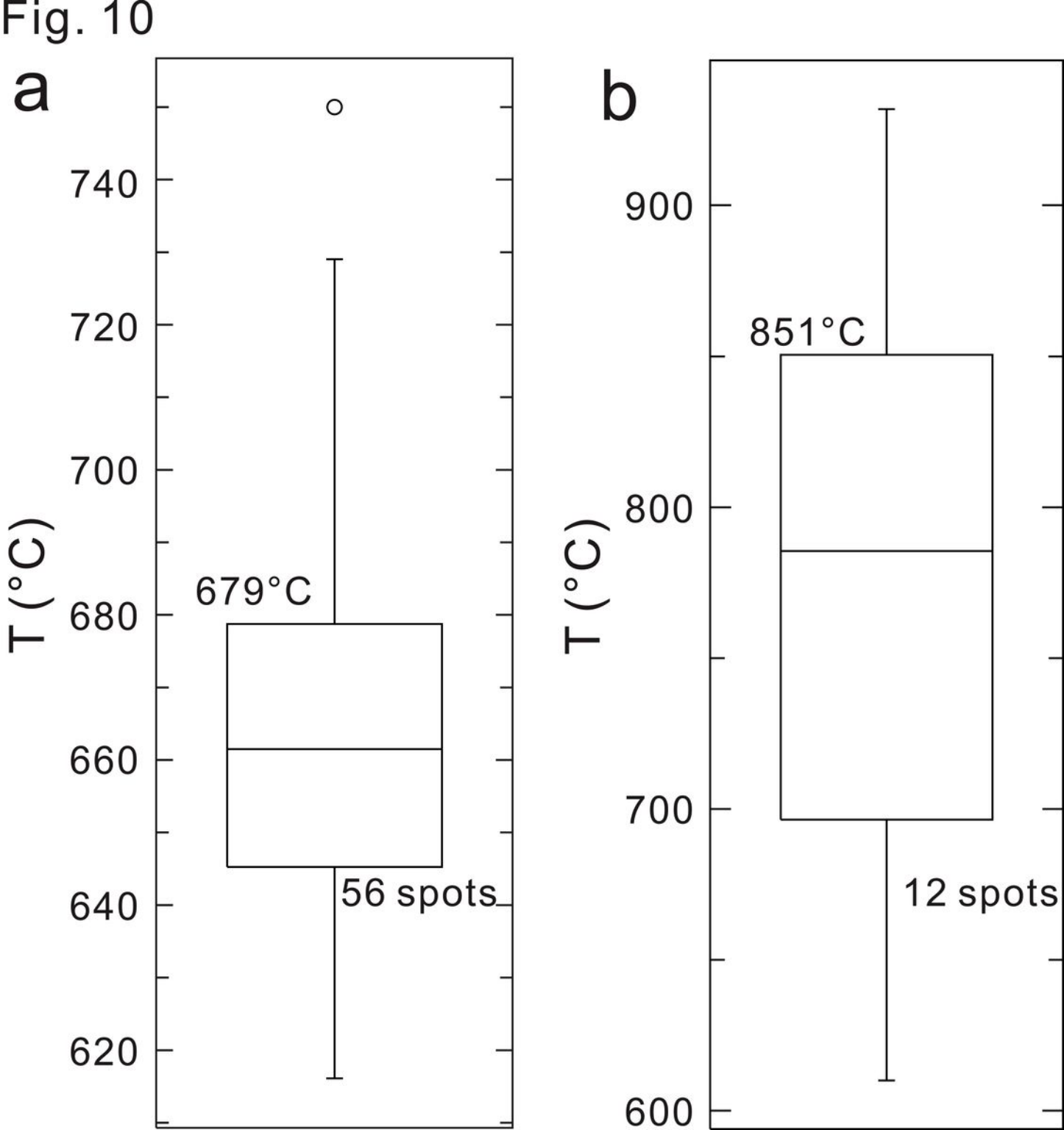
a
740
720
700
680
660
640
620
T (°C)
679°C
56 spots
b
900
800
700
600
T (°C)
851°C
12 spots

Fig. 11

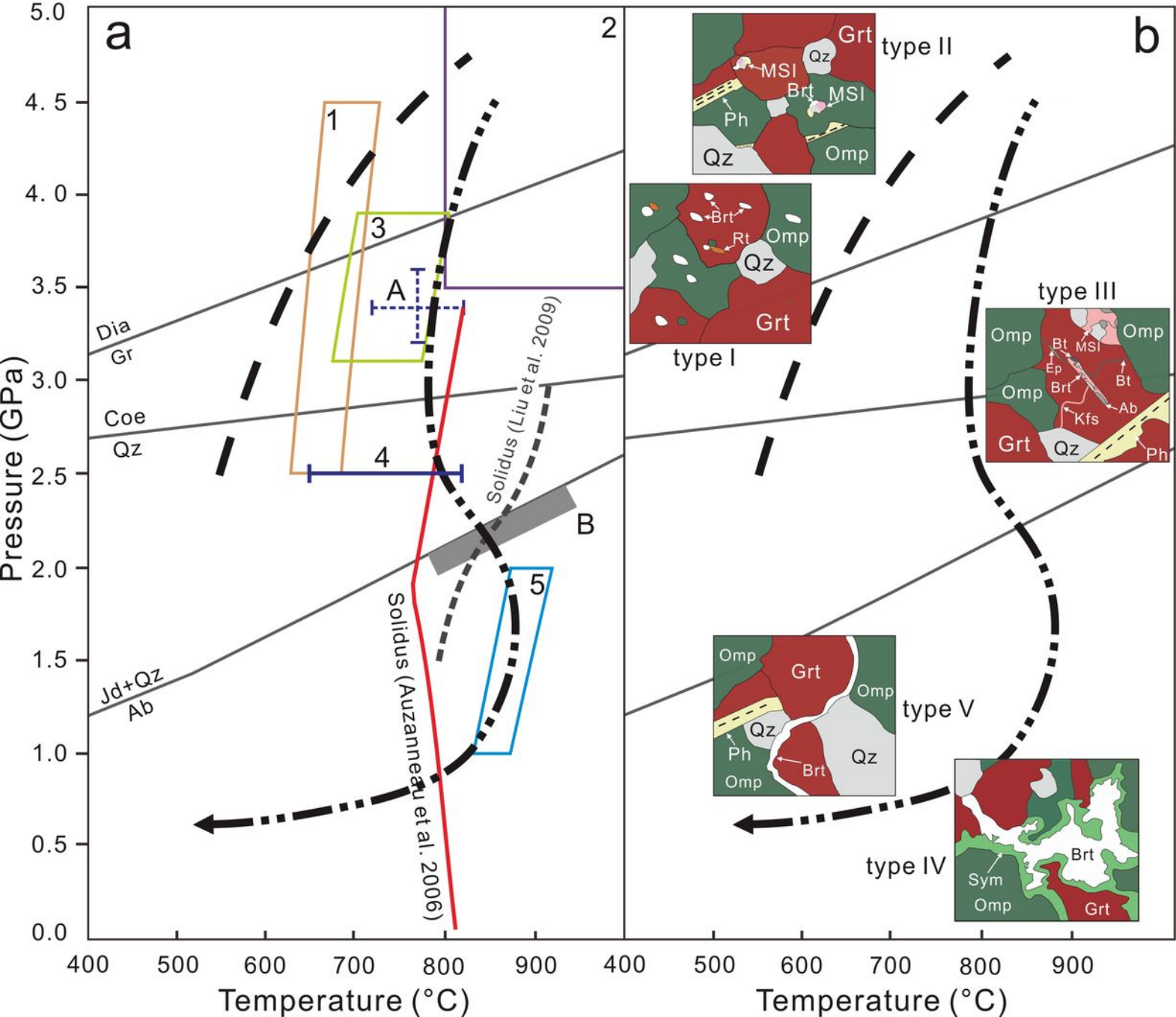
a
b
2
1
3
4
5
A
B
Dia
Gr
Coe
Qz
Jd+Qz
Ab
Solidus (Liu et al. 2009)
Solidus (Auzanneau et al. 2006)
Pressure (GPa)
Temperature (°C)
Temperature (°C)
type I
type II
type III
type IV
type V
Grt
Qz
MSl
Brt
Ph
Omp
Rt
Bt
Ep
Ab
Kfs
Sym